DOI:10.14753/SE.2024.2926

SEMMELWEIS EGYETEM

DOKTORI ISKOLA

Ph.D. értekezések

2926.

TÓTH ESTILLA ZSÓFIA

Funkcionális Idegtudományok
című program

Programvezető: Dr. Sperlágh Beáta, csoportvezető

Témavezető: Dr. Wittner Lucia, tudományos főmunkatárs

DOI:10.14753/SE.2024.2926

Different Aspects of Electrophysiological and Quantitative Electron Microscopic Investigations in the Rat and the Human Neocortex

PhD thesis

Estilla Zsófia Tóth

Neurosciences ("János Szentágothai") Doctoral School
Semmelweis University

Supervisor: Lucia Wittner, D.Sc
Official reviewers: Kozsurek Márk, PhD
Ábrahám Hajnalka, PhD
Head of the Complex Examination Committee: Alán Alpár, MD, D.Sc
Members of the Complex Examination Committee: Borhegyi Zsolt, PhD
Dobolyi Árpád, D.Sc

Budapest
2023

Table of Contents

List of Abbreviations

ABC	avidin-biotin complex
CA	Cornu Ammonis
Ca^{2+}	Calcium ion
CB1R	Type 1 cannabis receptor
CB1R+	Type 1 cannabis receptor-positive
CB1R-	Type 1 cannabis receptor-negative
Cch	Carbachol
CCK	Cholecystokinin
DAB	3’3’-diaminobenzidine
F	Female
GABA	Ɣ-aminobutyric acid
GD	Gyrus Dentatus
GFAP	Glial Fibrillary Acidic Protein
L2/3	Layer 2/3
LFPg	Local Field Potential gradient
M	Male
mAchRs	muscarinic acetylcholine receptors
MEA	Micro Electrode Array
MEMS	Micro-electromechanical systems
MUA	Multi-Unit Activity
MTLE	Medial Temporal Lobe Epilepsy
NeuN	Neuronal Nuclei antibody
NoEpi	Non-epileptic patient group
NOSPA	Area that is not generated SPA in vitro
OMIII	National Institute of Mental Health, Neurology and Neurosurgery
PAG	Photoacid Generator
PB	Phosphate buffer
PV	Parvalbumin
PV+	Parvalbumin Positive
PV-	Parvalbumin Negative

ResEpi	Resistant Epileptic (The patient group with drug-resistant epilepsy)
SPA	Synchronous Populational Activity
TB	Tris Buffer
TBS	Tris Buffer Salt

1 Introduction

Nowadays, we have the opportunity to choose from a wide range of methods for investigating the brain. With technological advances, more and more rather complicated methods became widely available. It is crucial to choose the proper method for the right questions or combine multiple approaches.

In the two studies I will present in this dissertation, we have used a rodent model for testing the in vivo biocompatibility of a novel material that can be used for preparing electrodes used in neuroscience research and clinical application on human patients. This project was also deemed perfect for testing our automated cell counting method and quantitative electron microscopy method, which can be proven helpful in many of our studies regarding the human brain.

Animal models are highly valuable in research since many methods can’t be applied to human patients in vivo or the samples in vitro. But they are also limited in nature since the human brain differs from the most widely used rodent models and shows numerous unique qualities. Because of this, the translation of findings from animal models of diseases to the human equivalent is often unsuccessful.

One possibility to reduce the failure ratio of the translation is not just the development of novel models but the use of human brain samples in research. Our research team has the opportunity to receive surgically removed human brain samples from the National Institute of Mental Health, Neurology and Neurosurgery (OMIII) as part of a long-standing collaboration. The most significant value of these samples compared to post-mortem human samples is that we can carry out in vitro electrophysiological investigations followed by post hoc anatomical examinations.

We have the opportunity to receive samples from patients with drug-resistant epilepsy and those who had to undergo surgeries due to a brain tumour but did not show any sign of epilepsy or a seizure. With these two groups, we can discover the changes possibly caused by epilepsy.

1.1 Su8 Biocompatibility in vivo

1.1.1 Importance of the material choice in electrode manufacturing

To gain the best spatial and temporal resolution when imaging brain activity in vivo, we must apply invasive techniques, namely implanting electrodes directly into the neuronal tissue (1,2). To monitor the tissue for a prolonged period of time or stimulate it, we need chronically implanted devices. This technique is crucial both in basic and applied research(3,4) and also in clinical applications (epilepsy diagnostics, brain stimulation, e.g., in Parkinson's disease or Tourette's syndrome) (5,6)

Extracellular probes implanted into the neuronal tissue can record local field potentials (LFP) and multiunit activity (MUA) from neurons closer than approximately 50 µm (4). These devices can be either single electrodes or multiple channel ones like tetrodes or multiple electrode arrays (MEAs). MEAs can allow us to record a vast amount of information at a time, letting us carry out current source density analysis (7,8) and allowing us interfaces (9). To construct high-density MEAs, we need microelectromechanical systems (MEMS) technology.

The most commonly used material for such devices in vivo is silicon and silicon-based materials (Si, SiO, Si_3N_4). Silicon-based materials and noble metals are inert and non-toxic to the surrounding tissue (10,11). But it is important to note that silicon-based materials are stiff compared to the neuronal tissue. This can cause damage due to the constant movement of the brain (e.g., breathing, blood flow) and limit the long-term performance of the electrode.

One way to improve this problem is the application of more flexible materials and the manufacturing of more flexible devices that mimic the micro motions and pulsation of the brain (12). This might be able to limit the glial scar formation around the probe and immune response(13,14).

There are several polymer materials that can be used for manufacturing such devices for neuronal applications, such as polyamide, polydimethylsiloxane, perylene and SU-8 (14), there is limited data about the applicability of liquid Christal polymers (15), acrylate and thiolene-acrylate shape memory polymers(16) among others.

1.1.2 Biocompatibility of implanted devices

Invasive devices like implanted electrodes must have excellent biocompatibility(17,18). It is less critical for acute recordings since the tissue will only be connected to the material for a limited time.

With chronically implanted devices, it is essential that the probe can function long-term with a good signal-to-noise ratio. For research purposes, it is vital that the animals can be used for several months and for clinical application, where the devices must work for years so the patients do not have to undergo further surgeries.

Several different aspects need to be considered when talking about biocompatibility in tissues. For neuronal tissues, the stiffness of the device needs to be considered since the brain is a soft tissue that is constantly moving. A softer material might connect better to the neuronal tissue (19,20).

It is also crucial to note that a glial scar will form around the probe, if it is too thick, it can separate the electrode from the target cells both electronically and spatially, so limiting it is of high importance. The scar will form as an immune response mainly by astroglial cells because of the foreign material in the brain (21,22).

When talking about electrodes in the brain, our primary goal is to record signals from the neurons, for this, we need cells in the close vicinity of the device not further than 50 μm (23,24). It is essential that there are cell bodies in this region and that we can preserve synaptic contacts.

The biocompatibility of electrode materials is needed to be thoroughly investigated since they can be toxic to cells or too stiff for neuronal applications.

1.1.3 SU-8 material in the CNS and its biocompatibility

The SU-8 material is a great negative photoresist, which makes it possible to conveniently, rapidly and cost-effectively manufacture microelectrodes with it (25,26).

SU-8 has high thermal stability, great feature resolution, excellent aspect ratio, chemical inertness and high cross-linking propensity, improving the swelling often occurring with negative resist materials (27). It has been applied for in vitro electrophysiological experiments (28) and in vivo devices (29–31). For in vivo experiments, it has been used for recording nerve action potentials (32), and for measurements in the rodent brain both for depth electrodes and on the cortical surface (30,31). SU-8 can also be used to manufacture microelectrode arrays with microfluidic channels (33,34). Because of the high transparency of the material, it is also possible to use it as a waveguide for optogenetic investigations (35,36).

1.1.4 Light microscopic and quantitative electron microscopic investigations for testing the biocompatibility of SU-8

The SU-8 material might be hurtful to neurons because of its manufacturing process (including chemicals such as PAG (Photoacid Generator) and antimony salt) (37).

Untreated SU-8 was shown to be toxic in cell cultures (38) due to toxic leachates. Several ways to improve its biocompatibility including heat treatment, isopropanol sonification, perylene coating or oxygen plasma treatment (38). In in vivo circumstances, it has been shown that antimony leaching is minimal and in the non-toxic region (39). ISO 10993 test, including chronic implantation in rabbit muscle for 1 to 12 weeks, has deemed SU-8 a non-irritant material (11). In subcutaneous application, it is known to cause minimal damage with minimal interaction with the surrounding tissue and to have high biocompatibility (18,39).

Despite previous efforts, detailed neuronal biocompatibility studies are lacking. In acute experiments, the material's flexibility was tested, causing limited damage compared to more rigid materials (34).

For a two-week-long implantation period, proper neuronal preservation and low glial response were shown, but this study only uses 2 rats and lacks quantification (40), similar results were presented from implantation into the mouse brain (41) with reliable recordings.

A more extended implantation period (e.g., two months) and a higher sample number is needed to gain reliable data about the material's biocompatibility.

In an experiment like this, the animals are sacrificed after the prolonged implantation period, and the brain tissue is fixed for pot-hoc anatomical investigations.

It is crucial to investigate both neurons and glial cells. For this purpose, the best method is carrying out immunohistochemical stainings, such as NeuN (Neuronal Nuclear Antibody) for targeting neuronal cells and GFAP (Glial Fibrillary Acidic Protein) for targeting astroglial cells.

Light microscopic measurements can give us a picture of the decrease in neuron numbers around the probe and the level of gliosis, and the thickness of a glial scar. However, such investigations are not suitable for determining whether synaptic contacts are preserved, determining the amount of glial elements around the electrode, and investigating the general ultrastructure of the surrounding tissue. For this reason, it is highly recommended to carry out electron microscopic investigation since it is well-quantifiable and is sufficient to determine whether recording a stable electrical signal would be possible.

Deeming a material highly biocompatible, safe, non-toxic, and resistant to damage caused by the tissue is crucial before using it in clinical applications. With the rapid improvement of manufacturing and data science, it became possible to start developing such electrical devices for human patients. One potential application is in epilepsy, where implanted and surface electrodes are often part of the diagnostic process. There are groups trying to apply deep brain stimulations for the treatment of epilepsy, this would include both recording the activity, then analysing it and giving stimuli when needed with chronically implanted devices. A damage-resistant material with high biocompatibility is essential for such application. The most commonly used silicon-based material can be a good candidate, but it is necessary to investigate whether other materials might be applied too.

1.2 Electrophysiological and anatomical examination of the perisomatic inhibition of Layer 2/3 pyramidal cell is the epileptic and non-epileptic human brain

1.2.1 Epilepsy

Epilepsy is one of the most common neurological disorders, affecting around 50 million people worldwide of all ages (42). The disease manifests in the form of seizures. It is presented in the brain as a neuronal hypersynchrony, causing the formation and recurrence of paroxysmal activity, including interictal spikes (noticeable on brain imaging) and spontaneously forming seizures (42,43). The term epilepsy is regarding many pathologies that can have genetic causes (mostly childhood epilepsies), including brain malformations during development (44). Childhood febrile seizures, traumatic brain injuries, alcohol and drug abuse. brain tumours, stroke, and ischemia can all play a role in the formation of epilepsy (42,44). Epilepsy can also appear in adults sporadically without a clear cause (43).

The diagnostic process includes different non-invasive brain imaging techniques such as EEG, CT, and MRI (45).

Epilepsy can affect different parts of the brain. The seizures can include the whole brain, like generalised tonic-clonic seizures or absence seizures (mainly in children). It is also possible that the seizures only affect certain areas, in these cases, the events can have smaller, vastly different manifestations (42,44,46). It is also possible that the seizure focus is well defined and the partial seizures become secondary global ones.

Epilepsies can be classified based on the location of the seizure onset zone. For adult epilepsies, the most common type is the temporal lobe (TLE) or medial temporal lobe epilepsy (MTLE), when the seizures originate either from the temporal cortex or the hippocampus(44,47).

The areas where the seizures initiating from are called the seizure onset zone. It can be located in the same area, or the seizures can start in different regions of the brain.

In many cases, the seizures can be well managed by anti-seizure medication. There are several different drugs available targeting mainly neuronal cells (46).

However, even in complex medication combining multiple drugs, approximately one-third of the patients are drug-resistant, meaning they have recurring seizures even with medication (often less than without it) or experience severe side effects (48).

TLE/MTLE patients are often drug resistant. Since, in this case, the seizure onset zone can be defined, one possible treatment is resective surgery (48). After detailed brain imaging, the seizure onset zone is defined and resected by a surgeon. It can include the temporal lobe and, in some cases, also the hippocampus. Resective surgery is also an option for other types of focal epilepsies. After surgery, many patients do not experience any major side effects in the long term. Approximately 50% of patients can be seizure free 5 years after the surgery, and up to 80% will experience a significant decrease in seizure frequency (49).

It is crucial to understand the neuronal basis of epilepsy to define new drug targets and gain a deeper understanding of the disease. One crucial step in this is understanding the role of different neuronal cell types in generating brain synchronies.

The epileptic reorganisation and role of different cell types in it and also in the initiation of synchronous activities are well researched, mainly in rodent models, and often in the hippocampus (50–53), It is important to note that we have considerably less data about the human brain (54,55).

1.2.2 Recent advances in human brain research

In recent decades, the investigation of surgically removed human brain samples has become more accessible with technological advances (e.g.: 2 photon microscopy, extra and intracellular electrophysiology). There is an ever-growing amount of data regarding the differences between the most commonly used rodent models and the human brain. Many research groups found differences in cell types (56–58) (physiology, protein expression, location and distribution), synaptic activities (59), glial cells (60), synchronous activities, and sub-cellular and network-level processes (61,62).

Based on this data, it is apparent that researching rodent models is not always sufficient. Including human samples in the research process is crucial to gain the whole picture and minimise the challenges arising during the translation of findings into therapies for human patients.

1.2.3 Physiological and pathological synchronies in the human brain in vitro

The balance of inhibition and exhibition in a specific brain area is crucial for forming physiological oscillation and synchronous events in human and rodent brains (63,64), playing an essential role in different cognitive processes like memory and sleeping. In epilepsy, this balance is thought to be disrupted, manifesting in the form of pathological synchronies (65), that can be recorded both in vivo and in vitro (52,66,67).

Physiological populational synchronisations and oscillations can be recorded in vitro in the hippocampus of many mammals (68), including rodents and humans.

On the other hand, the neocortex was long thought to be largely unable to form such activities in vitro in physiological circumstances.

So-called SPAs (synchronous populational activity) can be recorded in vitro both in epileptic and non-epileptic (tumour) surgically removed samples (69–72). It can be generated both in the neocortex and the hippocampus (I will discuss the neocortical SPAs). The emergence of SPAs is similar in different brain areas, and it is more frequently observed in epileptic than in non-epileptic tissue (73). Compared to inter-ictal like discharges (IID) which is a pathological manifestation in the epileptic brain in vitro, the SPA events are different in complexity, amplitude, and the participating and initiating cell types, and are thought to be a non-epilepsy related synchronous activity (66,73,74).

SPAs were not observed in any other species so far, including rodents and primates. To record this kind of activity, it is essential to investigate all cortical layers simultaneously, with close enough electrode contacts, to see the activity in multiple points and to cluster the cell firing during these events. This can also be the cause of why it has yet to be seen in any other species.

Recent data from human in vitro samples described both human-specific interneuron types (56) and unique connectivity roles (75) among the abovementioned observations.

Based on this literature data, it is also possible that these kinds of events are indeed human-specific, giving a different computational aspect in the neocortex.

SPAs are mainly similar in non-epileptic and epileptic samples. Still, differences in the occurrence rate, frequency and amplitude have been observed and might result from the higher excitability of the epileptic brain, also related to the emergence of paroxysmal activity (66,73).

1.2.4. Perisomatic inhibition and its role in the formation of synchronous events

The different types of inhibitory cells are important in controlling the various elements in the neuronal circuit. Interneuron-specific cells are important in disinhibition by blocking other interneuron types, axo-dendritic cells control the input of principal cells, while in contrast, perisomatic inhibitory cells are efficient in managing the output of the cell (not only on specific terminals but from the whole cell) (76,77).

The modulation of the output and activity of many excitatory cells quickly and efficiently is known to play an essential role in the formation of both physiological and pathological populational activities (synchronisations, oscillations, IID) (77).

For this reason, it is crucial to investigate the role of perisomatic inhibition in forming SPAs.

The Parvalbumin (PV) positive and the Cholecystokinin/ Type one cannabis receptor (CCK/CB1R) positive perisomatic inhibitory cells are two non-overlapping groups presented in several different brain regions (including the hippocampus and the neocortex) (77,78).

The PV-positive cells are axo-axonic (targeting the axon-initial segment) or basket cells (often fast-spiking), and the CCK/CB1R-positive ones are regular spiking basket cells. The basket cells form a typical basket-like formation around the cell bodies of principal cells, including layer 2/3 pyramidal cells consisting of many axon terminals in a single neuronal soma (79).

The fast-spiking perisomatic inhibitory cells play a crucial role both in physiological (80–82) and pathological (83–85) synchronisations. The PV-stained cells are essential in controlling rhythmic oscillatory activity in the brain, while CCK/CB1R positive ones are important in fine-tuning these events (77). CCK/CB1R cells also participate in multiple populational activities, including interictal spikes (86–90).

1.2.5 Parvalbumin positive innervation

Parvalbumin is a calcium-binding protein located in the cytosol of the basket and axo-axonic cells in both humans and rodents (91–93). PV-positive interneurons have a multipolar cell body with aspiny dendrites, which often cross through several cortical layers, many of their axons giving perisomatic synapses or coming from thalamocortical projections (93). The PV-cell are known to be affected by epilepsy in the hippocampus and the neocortex. The epilepsy-related changes in PV-positive cells in the hippocampus are rather complex, the number of stained somas is decreased, but in the Cornu Ammonis region, the perisomatic inhibition of the principal cells is preserved (94,95), meanwhile in the gyrus dentatus is even increased (96). It is important to note that their targets are also affected in an area-dependent way (97).

In the human neocortex, there seems to be a decrease in their density in epileptic samples (73,98,99). However, in the medial temporal gyrus in epilepsy, they were found to be unchanged (69). In abnormal neocortical areas from epileptic patients, a decrease in the amount of the inhibitory synapses and in the perisomatic inhibition has been shown (100).

1.2.6 Cholecystokinin/ Type 1 cannabis receptor positive inhibitory cells

In the human neocortex, CB1R is presented on the presynaptic axon terminals of a non-overlapping perisomatic inhibitory cell type which is also positive for cholecystokinin (a neurochemical marker) (77). In the rodent hippocampus, it is also present in asymmetric, presumably excitatory terminals (101). CB1R staining shows a layer-dependent staining pattern both in the human and in the monkey neocortex and shows an area-dependent staining (102). CB1R is only expressed in symmetric (presumably inhibitory) synapses in the monkey neocortex (102).

The epilepsy-related changes in the human hippocampus (drug-resistant MTLE) seem to be more complex- just like with the PV+ cells- the number of excitatory terminals is lower than the expression of CB1Rs (103). On the other hand, the inhibitory synapses showed an increased CB1R expression (104).

In the epileptic neocortex, the CB1R was overexpressed (105), but it was investigated in relation to malformations (dysplasia, glioneural tumour).

1.2.7 The role of the Cholinergic system in the modulation of the perisomatic inhibitory cells

Acetylcholine (ACh is an important neuromodulatory neurotransmitter in the CNS, with its receptors being present in many different brain areas. There are two types of ACh receptors the ionotropic nicotinic (nAChR) and the metabotropic muscarinic (mAChR) receptors. Acetylcholine plays an important role in functions like learning, memory, and arousal. It is also known to be changed in many different brain pathologies such as addiction, Alzheimer’s disease, Parkinson’s disease and dementia (106–108).

The cholinergic activation throughout nAChRs is shown to enhance GABAergic inhibition in the hippocampus and in the neocortex, both on excitatory and inhibitory cells (109), with numerous different signalling pathways (110). The effects via mAChRs can modulate the activity of pyramidal cells and perisomatic inhibitory interneurons (111).

There are 5 different mAChRs (M1 to M5) (112). In the rodent neocortex, activation via the M1 receptor inhibits Layer 5 pyramidal neurons (113) and is followed by a long-lasting voltage-dependent excitation (114,115). The M2 type mAChR is located on the axon terminals of PV-positive INs in the neocortex and is able to directly affect the GABA release by diminishing it (87,116,117). Around 75% of parvalbumin-stained cells in the human visual cortex contain the M1 receptor (118).

The cholinergic activation affects the CB1R-positive cortical interneurons in an indirect path. It decreases their GABA release through the postsynaptic M1/M3 receptors on their target pyramidal cells by triggering endocannabinoid release from them (87,119) resulting in the inhibition retrogradely on the presynaptic terminal (120–123).

1.2.8 Pharmacological modification to investigate the perisomatic inhibitory system in in vitro electrophysiology

One possible approach to investigate the role of different cell types in pathological or physiological processes is the modification through pharmacological agents in in vitro samples. By blocking certain cell types, pathways, or receptors, we can establish their role in forming certain events (such as SPAs).

Both in animal models of epilepsy and in human epileptic samples, in vitro mAChR receptors are involved in epileptogenesis (124–126).

Carbachol (Cch) is a non-selective acetylcholine receptor agonist. Via the M1 receptor, it can enhance the firing of pyramidal cells (115)and increase the temporal summation of information (127), through the M4 receptor, it reduces the amplitude of excitatory synaptic potentials (128). Also, able to decrease the release of GABA from interneurons (117,128) via the M2 mAChR. As mentioned above, Cch affects both nicotinic and muscarinic receptors, although, in vitro, its effects are known to be mainly muscarinic (128,129).

The pharmacon AFDX-116 is a selective M2 antagonist (130,131). In the human neocortex M2 receptor is selectively located on the axon terminals of PV-positive perisomatic inhibitory cells (132,133). The application of AFDX-116 can prohibit the effects of Cch selectively on PV-positive interneurons by rescuing them from the cholinergic activation.

AM-251 is a selective CB1R antagonist/inverse agonist. It can bind to CB2R also, but with a 306-fold lower affinity (134). CB1R is expressed in the brain, lungs, liver, and kidneys (135), while CB2R is mainly expressed on hematopoietic cells and in specific brain areas (amygdala, caudate/putamen, Nucleus Accumbens, cortex, hippocampus and cerebellum) (136). In the human neocortex, the CB1R is expressed both on excitatory and on inhibitory cells, but the expression is much stronger in the latter (137). It can block the indirect carbachol effect on CCK/CB1R positive terminals.

2. Objectives

My main interest during my doctoral studies and future projects is a more profound understanding of how the human brain works in the network, cellular and molecular levels and to investigate the background of neurological diseases in the human brain.

My main goal is to investigate human brain samples. I tried to get a sound basis for these investigations by getting experience studying rodent samples, perfecting our methods in these models and getting data that can be compared to the limited human research that can be carried out.

2.1 Su8 Biocompatibility in vivo

In vivo and vitro electrophysiological recordings are essential both in research and, in many cases in clinical applications.

Our Objectives in this study were to investigate the changes caused by a chronic 2-month long in vivo implantation of a device made from the SU-8 material into a rat brain. This material can be a good candidate for manufacturing micro electrodes because of its cost-effectiveness, photoactivity (for easy manufacturing), presumed non-toxicity, high flexibility and transparency.

We aimed to have a large sample size to be able to quantify our findings and carry out both light and electron microscopic investigations.

We chose probes without recording sites because we aimed to investigate the anatomical changes caused by the material.

Our research group carried out anatomical investigations on the light microscopic level. Based on these findings, we realised the need for a quantitative electron microscopic study (these findings will be explained in the results section, to help the understanding of the electron microscopic study that I carried out).

My objectives in this study were:

How does the general ultrastructure of the tissue change?

Are the synapses preserved around the track in close vicinity to allow us to record neuronal signals?

Is the glial scar that was observed at the light microscopic level actually as profound as it seems or not?

How many problems would this encapsulation cause in chronic implantations?

2.2 Electrophysiological and anatomical examination of the perisomatic inhibition of Layer 2/3 pyramidal cell in the epileptic and non-epileptic human brain

The involvement of perisomatic inhibitory cells in the formation and maintenance of synchronous brain activities is an already established phenomenon. However, we have a limited amount of data from human samples. The majority of the research in this field is focused on the hippocampus. Hence, we have a limited amount of data from the human neocortex.

As a continuation of previous studies in our lab (66,67,73) we aimed to investigate the SPAs in the human neocortex in vitro, with a focus on the involvement of perisomatic inhibitory cells.

We investigated two non-overlapping perisomatic inhibitory cell types, the parvalbumin-positive and the CCK/CB1R-positive inhibitory cells.

We carried out extracellular in vitro electrophysiological recordings and pharmacological modification with 3 drugs to investigate the PV+ and CB1R+ cells role in the generation of SPAs. We used the non-selective acetylcholine receptor agonist carbachol to block perisomatic inhibition, then selectively removed the two cell types from the effects of it. To target the PV+ cells, we used AFDX-116 to block the M2 receptors on them.

To target the CCK/CB1R+ cells, we used AM-251, a CB1R antagonist, to block the indirect effect of Cch on these cells.

We aimed to investigate how these pharmacons affect the SPAs in epileptic and non-epileptic samples (from tumour patients).

To further explore the possible changes in the perisomatic inhibition in the epileptic samples and the areas presenting SPAs, we carried out quantitative electron microscopic investigations with parvalbumin and CB1R immunostained samples separately. The SPAs were most often present in the supragranular layers of the neocortex. Hence, we chose layer 2/3 as our region of interest.

We investigated the cell bodies of the pyramidal cells located in these layers and measured the synaptic contacts made on them. We measured the amount of inhibitory contacts coming from a stained and unstained terminal, the overall coverage, the lengths of synaptic active zones and their number in 100 μm of soma perimeter.

3 Methods

3.1 Biocompatibility of the SU8

Since my main contribution to the project regarding the biocompatibility of the SU8 was mainly the electron microscopic investigation, I will only briefly describe the probes, the in vitro studies, and the light microscopic analysis.

The implanted non-recording SU8 probes were 5 µm thick and included a 3mm-by-3mm base for easier handling and a 5mm long 300 µm wide shaft ending in an angled tip (18°).

The in vivo biocompatibility of the probes was tested by a two-month-long implantation into both hemispheres of the brains of 31 Wistar rats (weight 220–500 g, 15 female and 16 male). The control samples from the study were obtained from distant brain regions from the same animals. The probes were implanted at the anterior-posterior (AP)-3 mm and medial-lateral (ML) 3mm coordinates in reference to the bregma.

Animals were kept and handled in accordance with the European Council Directive of 24 November 1986 (86/609/EEC), the Hungarian Animal Act, 1998 and the Animal Care Regulations of the Research Centre for Natural Sciences (RCNS).

3.1.2 Perfusion and sample preparation

After the two-month implantation period, the animals were anaesthetised with a cocktail of ketamine/xylazine (73 mg/kg and 10 mg/kg, respectively) and perfused with 300ml 4% paraformaldehyde and 15% picric acid solution in 0.1M phosphate buffer.

After removing the brains, they were cut into 60 µm-thick horizontal sections with the same vibratome as the human section. The following treatment of the slices was the same as described below in the 3.2.5.1 chapter (3.2.5.1 Immunohistochemistry) and as the human samples. We collected the slices starting from the pial surface and chose every 6th for GFAP staining and the remaining for NeuN (Table 1).

3.1.3 Processing of rat brain section images

We obtained good-quality samples from 21 animals (42 probe tracks), which were later included in the histological analysis (Table 1).

We have examined all sections at the light microscopic level to detect the probe track and further recorded at 2.5-, 5- and 10-time magnifications.

For the quantitative analysis of the samples, we have used an automated home-developed routine in MATLAB (The MathWorks, Natick, MA, USA). With this automated cell counting routine, it was possible to count the NeuN-stained cell bodies in 4 directions around the probe to determine the cell loss.

In the case of the GFAP sections, the average pixel density was measured in four directions around the track.

Table 1 The number of investigated samples in the light and electron microscopic investigations for NeuN and GFAP immunostained samples

	Number of animals	Number of hemispheres	Number of sections	Number of ROIs
Qualitative analysis of the implant track–light microscope				
NeuN	21	42	840	-
GFAP	21	42	154	-
Quantitative analysis of neuronal preservation – light microscope				
NeuN-	18	32	189	441
Quantitative analysis of astroglial reaction – light microscope				
GFAP	12	18	59	194
Quantitative analysis of synaptic density – electron microscope				
NeuN	3	3	3	9
GFAP	2	2	2	6
Quantitative analysis of the ratio of glial processes – electron microscope				
GFAP	3	3	3	9

3.1.4 Quantitative Electron microscopy of the rat samples

We conducted quantitative electron microscopic investigations based on the NeuN cell count results and the gliosis around the track (Table 1, Figure 1).

We have chosen three slices from three animals (2 left, 1 right hemispheres). The ROI was the area surrounding the track (Figure 1).

We analysed the density of synaptic contact in both stainings. We have determined 8 µm wide and 12 µm thick areas as the ROIs in three locations around the electrode track (Figure 1). We counted the synapses manually using ImageJ, and the density of synaptic contacts was normalised for a 100 µm^2 area.

The density of glial elements was measured with the same ROI structure up to 180µm from the track. We measured the area occupied by glial elements and divided it with the area of the sector.

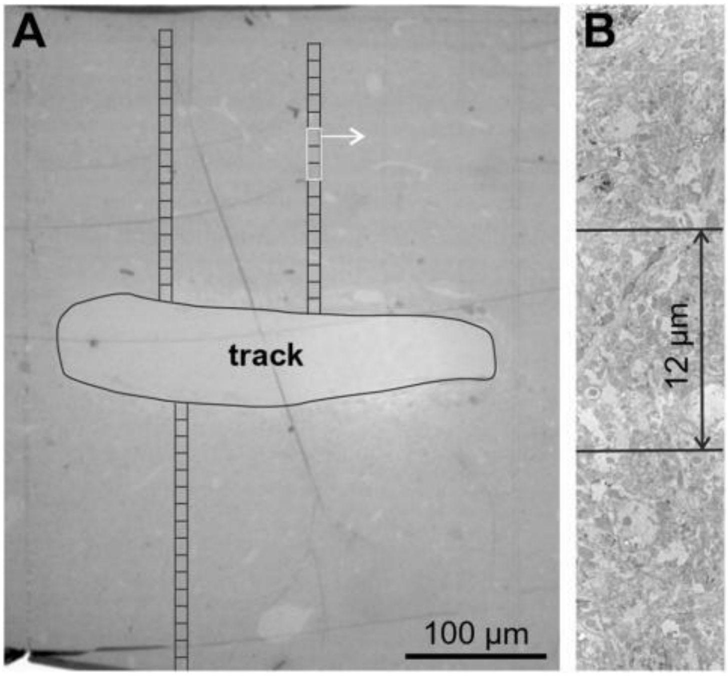

Figure 1. Quantitative electron microscopic analysis of the tissue surrounding the track of the SU8 probes. We have examined the ratio of glial elements, the density of synapses in the surrounding tissue, and the general ultrastructure. Around each track, we chose 3 places where we investigated the tissue for up to 192 µm distance from the probe, divided into 12 µm long, 8 µm wide ROIs (A), image B shows the area marked by white from image A on higher magnification.

3.2 Investigating the role of the perisomatic inhibitory system in the formation of SPAs in the human neocortex

3.2.1 Samples

Our research group has a longstanding collaboration with the OMIII. In this project, we have the opportunity to receive human brain samples from various types of brain surgeries. Approximately 30% of epilepsy patients are drug resistant. This means that the available drug treatment is either inefficient and the patient still has reoccurring seizures or severe side effects occur. If the seizure focus can be determined in these cases, one possible treatment option is resective surgery. These patients undergo a thorough pre-surgical evaluation (EEG, CT, MRI, and fMRI) (45), and based on these, the seizure onset zone can be determined. If it is resected, the majority of the patients will experience significant improvement, in 5 years after surgery, around 50% of patients are seizure-free, and up to 80% have a considerable seizure reduction (49).

We also have the opportunity to receive tissue samples from tumour surgeries. In these cases, the samples are not from the tumour but the surrounding tissue. The tumour patients, in some cases, can also have seizures (single or reoccurring). In this study, we only included patients with no seizures based on their anamnesis (proved with intra-surgical ECoG recordings when possible).

We acquired written consent from all patients before the surgeries. Our project was approved by the Hungarian Ministry of Health and by the Regional and Institutional Committee of Science and Research Ethics of the Scientific Council of Health (ETT TUKEB 20680-4/2012/EKU) and performed in accordance with the Declaration of Helsinki and by the hospital's internal ethics committee.

3.2.1.2. Non-epileptic patients

In this study, we used tissue from 13 non-epileptic patients (ages: 32-81 (60.5±14.2) (Table 2), who had undergone surgeries to treat their brain tumours. These patients did not have a history of epilepsy or seizures, based on their clinical anamnesis and further proven with intra-surgical ECoG recordings when possible.

The tissues originated from different brain areas as follows: n=4 from the frontal, n=5 from the temporal, n=3 from the parietal and n=1 from the occipital lobes (Table 2).

Based on preoperative imaging studies (MR), the obtained tissue was outside of the tumour zone in every case and had to be resected due to technical reasons, the distance from the tumour was classified as close if the distance was below 3cm or distant is it was above.

3.2.1.1 Epileptic patients

In this project, we have used tissue from 12 epileptic patients (ResEpi), ages: 28-53 (mean±st.dev: 37.8±7.7) (Table 2), suffering from pharmaco-resistant epilepsy for 22±15 years on average. One sample was from the frontal cortex, and 11 from the Temporal lobe. 8 samples were from outside the seizure focus but from areas where the seizures invaded. In 4 cases, the samples were from the seizure onset zone (Table 2).

The patient has shown different pathologies other than epilepsy (see Table 2), e.g., hippocampal sclerosis (n=4), focal cortical dysplasia (n=2), tumours (n=4), cortical gliosis (n=3) or stroke-induced lesions (n=1). All of our epileptic patients had therapy-resistant epilepsy.

3.2.2. Sample preparation

Our laboratory was located inside the hospital. The transportation of the samples from the operating room took less than 10 minutes. After the surgeon resected the tissue, it was immediately put in an ice-cold oxygenated sucrose-based cutting solution containing (in mM): 248 D-sucrose, 26 $NaHCO_3$, 1 KCl, 1 $CaCl_2$, 10 $MgCl_2$, 10 D-glucose and 1 phenol red, equilibrated with 5% CO_2 in 95% O_2.

Table 2. Patient data

Abbreviations: NoEpi: non-epileptic patients (samples from tumour surgeries), ResEpi: pharmacoresistant epilepsy patients, F: female, M: male, EM: electron microscopic investigations, PH: additional pharmacological examinations. We defined the distance of the tumour as close if the samples were from less than 3cm distance and distant if it was more than 3cm away. All samples underwent extracellular electrophysiological experiments (recording SPA events) and posthoc anatomical investigations involving immunohistochemistry followed by light microscopic studies.

Stage of epilepsy	**Gender**	**Age**	**Duration of epilepsy (years)**	**Histology/Diagnosis**	**Resected cortical region**	**Experiment**	**Seizure onset zone**	**Distance from tumour**	**Anatomy of obtained tissue**
NoEpi	M	81		glioblastoma multiforme grade IV	temporal	EM		close	infiltrated/ normal
NoEpi	M	32		anaplastic astrocytoma grade III	temporal	PH		close	infiltrated
NoEpi	F	63		lung carcinoma metastasis	occipital	PH		close	normal
NoEpi	M	64		lung adenocarcinoma metastasis	frontal	PH		close	compressed cortex
NoEpi	M	67		diffuse large B cell lymphoma	frontal	PH		close	normal
NoEpi	F	78		glioblastoma grade IV	temporal	EM, PH		distant	normal
NoEpi	F	65		glioblastoma multiforme	temporal	EM, PH		close	normal
NoEpi	F	52		glioblastoma grade IV	parietal			distant	infiltrated
NoEpi	F	36		anaplastic ependymoma grade III	parietal	PH		distant	normal
NoEpi	F	55		glioblastoma multiforme	frontal	PH		distant	normal
NoEpi	F	59		breast carcinoma metastasis	frontal			close	infiltrated
NoEpi	F	68		glioblastoma multiforme grade IV	temporal	EM		close	normal
NoEpi	F	67		glioblastoma multiforme grade IV	parietal			close	normal
ResEpi	M	39	35	hippocampal sclerosis	temporal	EM	no	-	normal
ResEpi	F	53	40	hippocampal sclerosis	temporal	EM	no	-	normal
ResEpi	M	35	34	focal cortical dysplasia + hippocampal sclerosis	temporal	EM	no	-	normal
ResEpi	M	32	23	focal cortical dysplasia IIb with balloon cells	temporal	EM	no	-	normal
ResEpi	F	41	9	hippocampal and cortical gliosis, microglia activation	temporal	EM	no	-	dysgenetic
ResEpi	F	34	3	cortical gliosis	temporal	PH	yes	-	normal
ResEpi	M	37	19	cortical gliosis, microglia activation	temporal	PH	no	-	normal
ResEpi	M	32	19	ganglioglioma grade I	temporal		yes	close	normal
ResEpi	M	30	6	hippocampal sclerosis, reactive astrocytosis, microglia activation	temporal	PH	no	-	normal
ResEpi	F	28	27	diffuse glioneural tumour grade I	temporal	EM, PH	no	distant	normal
ResEpi	F	48	10 months	diffuse astrocytoma grade II	temporal	PH	yes	close	normal
ResEpi	M	45	43	stroke-induced lesion	frontal	PH	yes	distant	dysgenetic

After removing the pia and the external blood vessels, we cut the 500 µm thick slices from the tissue blocks using a Leica VT1000S vibratome (Leica Biosystems, Buffalo Grove, IL, USA, RRID: SCR_016495). We only used slices that contained all 6 cortical layers.

The slices were kept in an interface chamber at 35-37°C filled with standard artificial cerebrospinal fluid modified for human samples (in mM: 124 NaCl, 26 NaHCO3, 3.5 KCl, 1 MgCl2, 1 CaCl2, and 10 D-glucose) equilibrated with 5% CO2 in 95% O2.

3.2.3 Extracellular recordings

We have recorded the extracellular Local Field Potential gradient (LFPg) with a 24-channel laminar microelectrode (inter-contact distance: 150 µm, (73,95,138) and a custom voltage gradient amplifier of passband 0.01 Hz to 10 kHz. LFPg is defined as the summation of dendritic potentials (both excitatory and inhibitory) originating from several neurons located around the electrode site (139,140). We have digitalised the signal with a 32-channel, 16-bit resolution analogue-to-digital converter (National Instruments, Austin, TX, USA) at a 20kHZ sampling rate. We have used a home-written routine for the recordings in LabView8.6 (National Instruments, Austin, TX, USA, RRID: SCR_014325).

The 24 channels with the 150 µm contact distance allowed us to record from all 6 cortical layers by putting the electrode on the sample perpendicular to the layers. Usually, we set up the electrode so that the 1-12 contacts were located on the supragranular layers, 13-15 on the granular and 16-24 on the infragranular layers and, in some cases, on the white matter. The slice was mapped by recording every 300-400 µm from one end to the other, and this allowed us to determine the areas showing SPA or not and also which layers are expressing it. We used this data to carry out the post hoc anatomical examinations.

When we could record stable SPAs (present for more than 10 minutes without any apparent changes), we conducted pharmacological experiments targeting the perisomatic inhibitory cells. First, we applied carbachol (5 or 10 µM in ACSF, 100 ml Merck, Kenilworth, NJ, USA), a non-selective acetylcholine receptor agonist, for about 20-30 minutes. After a washout period with ASCF (approximately 30 minutes or 100ml), we used different pharmacons targeting the various subtypes of perisomatic inhibitory cells. For blocking PV-positive inhibitory cells, we used AFDX-116 (10 µM, 50 ml, Tocris Bioscience, Ellisville, Missouri, USA), an M2 muscarinic acetylcholine receptor agonist. For blocking CB1R/CCK positive cells, we used AM-251(1 μM, 50 ml, Tocris Bioscience, Ellisville, Missouri, USA), a CB1R antagonist. First, we applied the antagonist on their own, then together with carbachol. Lastly, we had a 30-minute-long recovery period with ACSF. We recorded 10-minute-long epochs during the pharmacological experiments: control – carbachol – washout N°1 – mAChR antagonist – mAChR antagonist with carbachol – washout N°2.

3.2.4 Electrophysiological data analysis

We have used the Neuroscan Edit 4.5 program (Compumedics Neuroscan, Charlotte, NC, USA) and home-written Matlab routines (The MathWorks, Natick, MA, USA, RRID: SCR_001622) for detecting and analysing the SPAs. Before analysis, we supervised and corrected the electrode contacts' locations when needed.

We detected the SPAs on the LFPg recordings Hamming window spatial smoothing and band-pass filtering between 1 and 30 Hz (zero phase shift, 48 dB/octave). The LFPg amplitude of the events were determined on band-pass filtered 1-30 Hz recording. We have only included the SPA events in the recordings if their LFPg amplitude was at least two times the standard deviation of the baseline activity. In the following, I use the term SPA as the totality of events in a given recording (average 286±214 SPA events/recording). The event’s laminar location can vary but is most common on the superficial layers of the neocortex (we have always noted the location of the electrode contacts base on pictures made during the recording).

Time zero for the averaging was determined as the most prominent LFPg peak of the events.

We also determined the location and the recurrence frequency for the recordings during the entirety of the experiment. To investigate the changes in the LFPg amplitude caused by the pharmacon, we used both the averaged LFPg amplitude and the so-called ‘individual LFPg amplitude’ which we defined as the amplitude of the separate events present in a recording. We detected the individual LFPg amplitude on the channel, which showed the largest LFPg amplitude.

We calculated the multiple unite activity (MUA) as follows (73).

We averaged both LFPg and MUA from -300 to +300 ms from point zero of the events.

We applied baseline correction from -150 to -50 ms to averaged LFPg and MUA.

We represent the data using the median [1st – 3rd quartiles] form. At the same time, the changes caused by the pharmacon are presented as percentages compared to the baseline in ACSF.

3.2.5 Histology

3.2.5.1 Immunohistochemistry

After the physiological recordings, the slices were fixed overnight in 4% paraformaldehyde and 15% picric acid dissolved in 0.1M phosphate buffer (PB). The next day we washed the slices 3 times with 0.1M PB and put them in 30% sucrose solution overnight. The slices were frozen over liquid nitrogen 3 times (for permeabilising the membranes for the immunohistochemistry). The slices were recut by embedding them in 2% agar-agar using a Leica VT1200S vibratome into 60 μm thin slices.

The immunohistochemistry was the same on the rat and the human brain slices.

Unless stated otherwise, all the steps were carried out in a 0.1% PB solution.

The slices were washed in 0.1M PB 3 times for 10 minutes each and incubated with 1% H_2O_2 for 10 minutes to block the endogenous peroxidase activity. After one washing step for 10 minutes, we incubated the samples with 2% normal goat serum and 2% normal horse serum for 1 hour to block the aspecific antibody binding. After one 5-minute wash, the slices were incubated with the primary antibody (see details at the end of the sub-chapter) for two days at 4°C.

On the third day, we washed the slices three times for 10 minutes, and then we incubated the slices in the biotinylated secondary antibody for 2 hours in a 1:250 dilution. The secondary antibody that we used was from the same species as the primary antibody, either anti-mouse or anti-rabbit IgG (Vector, Burlingame, CA, USA). Following three 10-minute washes, we incubate the samples in avidin-biotinylated horse-radish peroxidase complex (ABC, Vector) in 1:250 dilution for 1.5 hours. After 3 10-minute washes, the immunoperoxidase reaction was developed by 3,3'-diaminobenzidine tetrahydrochloride as a chromogen, 20 minutes pre-incubation in the dark, then we added 10μl of 1% H_2O_2 to the solution and developed the samples according to the antibody.

After 3 washes, the samples were dehydrated, so it was possible to carry out electron microscopic investigation in the future.

We incubated the slices in 0.25% OsO_4 for 20 minutes in the dark, followed by three 10-minute washes. The slices were dehydrated in alcohol: 50%, 70% and 90% for 10 minutes each, absolute alcohol two times for 5 minutes, and finished with acetonitrile two times for 7 minutes. After the last step, the slices were covered in Durcupan (AMC, Fluka) overnight. The next day we mounted the slices onto microscope slides and incubated than at 60°C for two days in a heating cabinet to polymerise the Durcupan.

Some of the rat slices were only dehydrated for light microscopy. In this case, we mounted the sections onto microscope slides from chrome gelatine, immersed them in Xylene twice for 10 minutes each, and finally mounted them in DePex (Serva).

Both on the rat and the human slices, we have carried out NeuN antibody (1:2000, EMD Millipore, Billerica, MA, USA, RRID: AB_2298772) and glial fibrillary acidic protein antibody (GFAP, 1:2000, EMD Millipore, Billerica, MA, USA, RRID: AB_94844) stainings to visualise the neurons and the glial cells respectively.

On the human samples, we also carried out Parvalbumin (PV 1:7000, Swant, Bellinzona, Switzerland, RRID: AB_10000343) and CB1R (1:800, Cayman Chemicals, Ann Arbor MI, USA, RRID: AB_10080036), stainigs to visualise two distinct types of perisomatic inhibitory cells.

3.2.5.2 Sample preparation for electron microscopy

After light microscopic investigations, we chose the region of interest (ROIs) for the electron microscopic examinations.

In the case of the SU8-implanted rats, we have chosen the part of the slices that contained the electrode track in the GFAP and the NeuN stained sections.

In the case of the human slices, PV and CB1R stained slices were chosen, with two ROI from each slice, one from the area where we have been able to record SPAs and one outside of it (the areas were investigated but have not shown SPAs), as far from the former as possible. Both the SPA and the NoSPA samples contained the 2. and 3. cortical layers (L2/3).

We re-embedded the ROIs for electron microscopy. We prepared ultra-thin 55-70 nm thin sections with the Leica EM UC7 ultramicrotome (Leica Biosystems, Buffalo Grove, IL, USA, RRID: SCR_016694). The ultra-thin serial sections were collected on Formvar-coated copper slot grids (both the Formvar and the grids Electron Microscopy

Sciences, USA, we have prepared the coting ourselves). The samples were treated with lead citrate for 2 minutes, followed by a distilled water wash.

The sections were visualised either with a Hitachi 7100 electron microscope (Hitachi Ltd., Tokyo, Japan) for the rat tissue samples and preliminary studies on the human samples) or a Jeol JEM-1011 (Jeol, Tokyo, Japan) (for the quantitative analysis of the human slices). In both cases, we have used the Mega-View III digital camera and a Soft Imaging Solutions (Olympus, Tokyo, Japan) image analyser system.

3.2.5.3 Electron microscopic investigations of Layer 2/3 human cortical pyramidal cells

We have taken electron micrographs of the cell body of every L2/3 pyramidal cell in our samples, as well as all the boutons terminating on them in higher magnifications. We have distinguished the pyramidal cells based on their size, shape, electron density, and nucleus. Interneurons tend to have more invaginated nuclei and a lower nucleus/cytoplasm ratio, and their cytoplasm is less electron-dense than the pyramidal cells. We have determined each synapse's inhibitory/excitatory nature (based on their symmetric or asymmetric appearance). Glial cells are usually more electron-dense than neurons.

We have sorted the presumed inhibitory terminals into two groups based on their immunopositivity, the CB1R and the PV-stained section were analysed separately. We only examined one ultrathin section per ROI to avoid the double sampling of cells and terminals.

We have measured the perimeter of every cell and the length of all the synaptic active zones on the cell bodies. We have used the Image J program (National Institute of Health, Bethesda, MA, USA) for the measurements. We have calculated the number of synapses/ 100 µm soma perimeter, the synaptic coverage (µm of synaptic active zones/ 100 µm soma perimeter) and the average length of the individual active zones/cell. We have calculated both measurements for stained and unstained synapses and also combined, separately, for CB1R and PV (PV/SPA+, PV/SPA-, CB1R/SPA+, CB1R/SPA-).

We have examined 123 cells from PV-stained sections from 3 Res Epi and 3 NoEpi patients and 157 in CB1R stained slices from the same amount of patients at the electron microscopic level. The number of pyramidal cells was between 7 and 18 (average 11.7±3.7) per ROI.

3.3 Statistical analysis

For the analyses of the histological data, we have used the Statistica 13 program (Tibco Software Inc. Palo Alto, CA, USA, RRID: SCR_014213) both for the human and rat samples. In every case, we started with the normality analysis (Kolmogorov-Smirnov & Lilliefors test) and decided the further used probes based on whether the data followed a normal distribution. We have defined a significant difference as $p<0.05$ ($p<0.05$ is * and $p<0,001$ is **).

3.3.1 Human quantitative electron microscopy

In all cases (total, PV+, PV-, CB1R+, CB1R-), the lengths of the synaptic active zones followed a normal distribution. We have used the Student's t-test to determine whether the statistical differences are significant or not.

Since the number of synapses/100 µm and the synaptic active zone length/100 µm did not follow the normal distribution, we used the Mann-Whitney U test to compare two groups and the Kruskal-Wallis ANOVA test for multiple comparisons. In the case of the Kruskal-Wallis ANOVA test, we corrected the p values with the Bonferroni adjustment.

3.3.2 Histology and quantitative electron microscopy of the rat brain samples

Since none of the data from the rat samples showed normal distribution, we used the Kruskal-Wallis ANOVA test.

3.3.3. Human Electrophysiological data

We have used the R software to test the statistically significant differences in the electrophysiological data (R Core Team 2020, R Foundation for Statistical Computing, Vienna, Austria). Based on the Shapiro-Wilk test, the data did not follow the normal distribution. We have used the One-way Repeated Measures ANOVA test to reveal the possible differences caused by the pharmacological agents within the patient groups (ResEpi and NoEpi, separately) in the frequency, LFPg- and MUA amplitude. We have used the post hoc multiple, pairwise paired t-tests with a Bonferroni adjustment to determine pairwise differences. To reveal the significant differences between the NoEpi and the Res Epi patient groups regarding the frequency, LFPg- and MUA amplitude, we have used Welch's t-test.

4. Results

4.1 Biocompatibility of the Su8 material

I will only briefly describe the implantation and the light microscopic result since this part of the project was not carried out by me, but it is important to explain before the electron microscopic studies.

4.1.1 Implantation and surgical complications

Our collaborators manufactured the implants. The above-mentioned electrode configuration was able to penetrate the brain after the dura was cut, and the probe was also flexible enough to minimise brain damage.

During the two-month implantation period, bleeding and subsequent damage occurred in 9 hemispheres of 6 animals, probably due to the animals hitting their heads. These samples were excluded from the analysis since the aim of this study is to explore the biocompatibility of the SU8 material, and the bleeding is not connected to it.

4.1.2 Light microscopic studies around the device track

We have investigated 441 ROIs from 189 sections from 18 rats on the light microscopic level. We have analysed the data based on its distance from the probe. We regarded the area 200–400 μm from the track as the control region (figure 2 shows that both the neuronal and the glial distribution can be assumed to be normal). As expected, the astroglial cells showed a relatively uniform distribution across the different cortical layers (141). Meanwhile, the neurons have shown a rather characteristic layered distribution(142,143). Sparsely staining in the first layer, densely packed cells in layers 2 and 4, and larger cell and lower neuronal density in layers 3,5 and 6.

4.1.3 Neuronal survival around the implant track

The decrease in neuronal density was considerable in the two closest ROIs, 24% (0.24±0.28) at 20-40 μm and 74% (0.74±0.39) between 40-60 μm compared to the control region (200-400 μm, 1.00±0.22) (Figure 2). At a further distance, the neuronal density was not significantly different (Figure 2).

Figure 2. Light microscopic investigations of the neuronal cell loss around the chronically implanted SU-8 probes

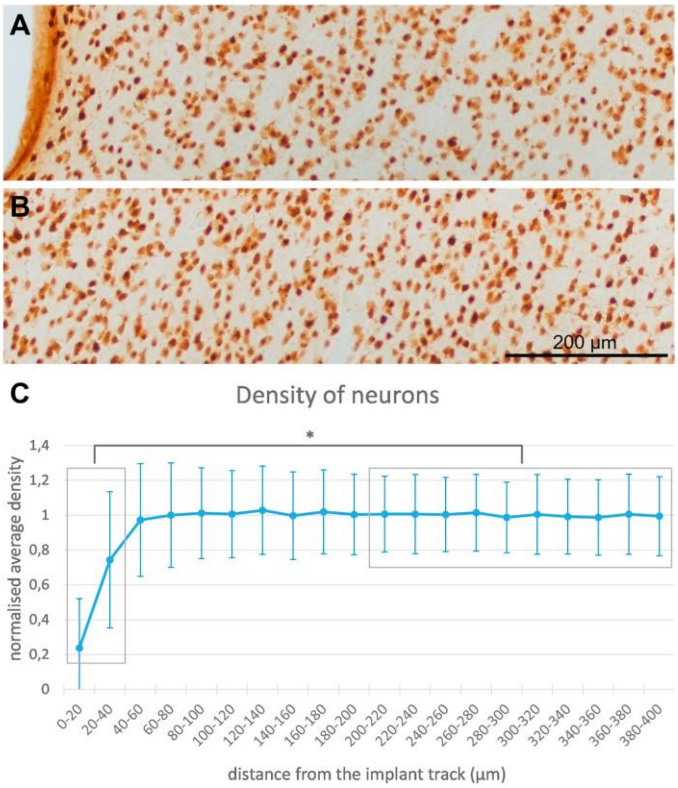

A: NeuN stained cells near the electrode track (visible as a white hole on the left). B: Neurons in a control area 1mm from the device. C: Quantified neuronal loss depending on the distance from the probe. The area between 200-400 µm distance was regarded as control. The two closest areas (0-20 µm and 20-40 µm) showed a significantly decreased neuronal density ($p<0.05$). At 40 µm and further, the density was comparable to the control. * shows the significant differences. The boxes indicate the control area (on the left 200-400 µm) and the area that was significantly different. ((144), Modified from Kinga Tóth)

4.1.4 Formation of a glial scar around the track

We have examined 194 ROIs in 59 sections from 12 animals.

We investigated a longer distance from the track (up to 800 µm), where the 600-800 µm distance was regarded as the control (Figure 3). There were no significant differences based on hemispheres or the side of the track, but we found a difference based on the cortical depth in the glial scar. We examined layers 1-3 and 4-6 in two different groups, the layers were determined based on the NeuN staining (Figure 3). We have measured the pixel density as a sign of a glial scar or density change (where the lower numbers indicate the stronger staining). We have found a significant difference between the superficial and deep layers up to 240 µm from the track, and it was more pronounced in the superficial layers ($p<0.05$, 0.29±0.14 to 0.81±0.15 in the supragranular layers and 0.44±0.21 to 0.87±0.17 in the granular and infragranular ones, Figure 3). At longer than 240 µm distance, there were no significant differences between layer1-3 and layer 4-6 ($p>0.05$, 0.85±0.14 and 0.90±0.15 in the superficial, 1.01±0.03 and 1.02±0.19 in the deep layers, Figure 3).

Compared to the control areas found a significantly stronger glial staining up to 560 µm from the track in the supragranular layers (0.29±0.14 at 20-40 µm and 0.98±0.06 at 520–560 µm from the probe, Figure 3).

In the case of the deep layers, we found a significantly stronger staining up to 480 µm from the probe compared to the control areas (0.44±0.21 at 0–40 µm and 0.99±0.18 at 440–480 µm distance, p<0.05, Figure 3).

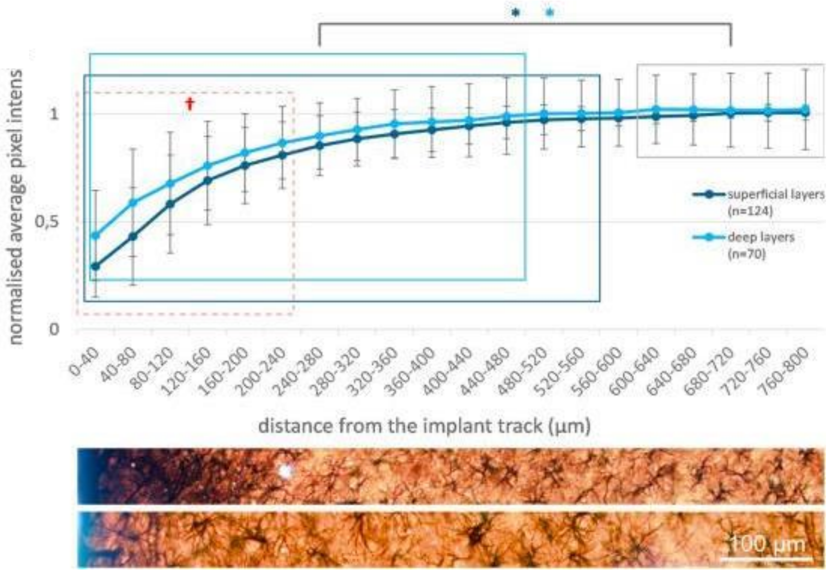

<u>Figure 3</u> Quantification of the GFAP staining intensity based on the difference from the probe and the cortical depth.

A lower pixel intensity on the y-axis indicates a stronger GFAP staining. The data were normalised to the control region in the 600-800 µm distance (grey box). In close proximity to the probe (closer than 240 µm), there was a significant difference between the superficial and the deep layers, the previous showing a stronger reaction (red-dashed box, red cross). We found a significantly (*) stronger staining in both groups compared to the control area. In the superficial slices, it was present up to 560 µm (dark blue box), while in the deep ones, it was recorded up to 480 µm (light blue box). The bottom images show examples of the investigated areas from superficial and deep layers respectively the probe being on the left. ((144)Modified from Tóth Kinga)

<u>4.1.5 Quantitative electron microscopy around the probes</u>

In the case of biocompatibility studies, the light microscopic investigations are not sufficient on their own. Although they give great insight into the decrease in neuronal cell bodies and the increase in the glial cells, we cannot gain information about the ultrastructure, the amount of glial elements and synapses. Since the goal of the chronically implanted extracellular electrodes is to get a strong and long-lasting signal, it is vital that the synapses around the electrode can survive and that the glial scar around the track is not too thick since it can limit the quality of the recordings (145).

To gain a deeper understanding of the structural changes around the probes, we carried out transmission electron microscopic investigation. We studied the general ultrastructure (Figure 4), the synaptic connections (Figure 5), and the changes in the amount of glial elements (Figure 6). This data can give a great insight into whether we would be able to record biologically relevant, stable, and strong signals through the implantation period. We have been able to quantify the number of synaptic elements.

The stronger GFAP staining around the track can also happen because of technical reasons. Namely, the strongest signal is always present at the tissue-liquid interface since it is the easiest for the antibody to penetrate. Generally, the immunohistochemical stainigs are the strongest on the upper and lower surface of the 60 μm thick sections, but in this case, we had a secondary contact site in the probe path. This partially explains why the staining seemed more pronounced around the track. To exclude this phenomenon from our data, we have measured the amount of glial elements at the electron microscopic level depending on the distance from the probe.

4.1.5.1 General ultrastructural changes around the track

We found a 2.5-15 μm thick glial scar around the probe in all 3 samples (Figure 4, A, B). In close vicinity to the probe, we have seen a high number of damaged elements in the neuropil. The characteristics of these elements were disrupted membranes with a low amount of cellular organelles or a complete lack of them (Figure 4 D, E). This suggests that these elements were not able to function properly.

The amount of damage varied between the samples. The damage was more pronounced in two of the three cases than in the third one. The glial scar was 5-15 μm thick in these two samples. We found numerous caverns in the tissue up to 50 μm from the track as a sign of tissue damage. Up to a 30-40 μm distance, we could find neuronal cell bodies, but they had a distorted shape (oval somas, presumably from the compression caused by the implant, Figure 4). In the third sample, the glial scar was thinner (2.5 μm), and caverns were less numerous and only reached approximately 30 μm from the track. The distorted cell bodies were present at a distance of 10-15 μm. At distances greater than 50-100 μm, we found round seemingly healthy-looking NeuN-stained cell bodies

(Figure 4, C, D, E). The caverns were sporadic at this distance. The tissue has also shown a great number of healthy elements, such as dendrites, axons, and synapses (Figure 4, C, D, E).

Notably, the caverns were not detectable at the light microscopic level.

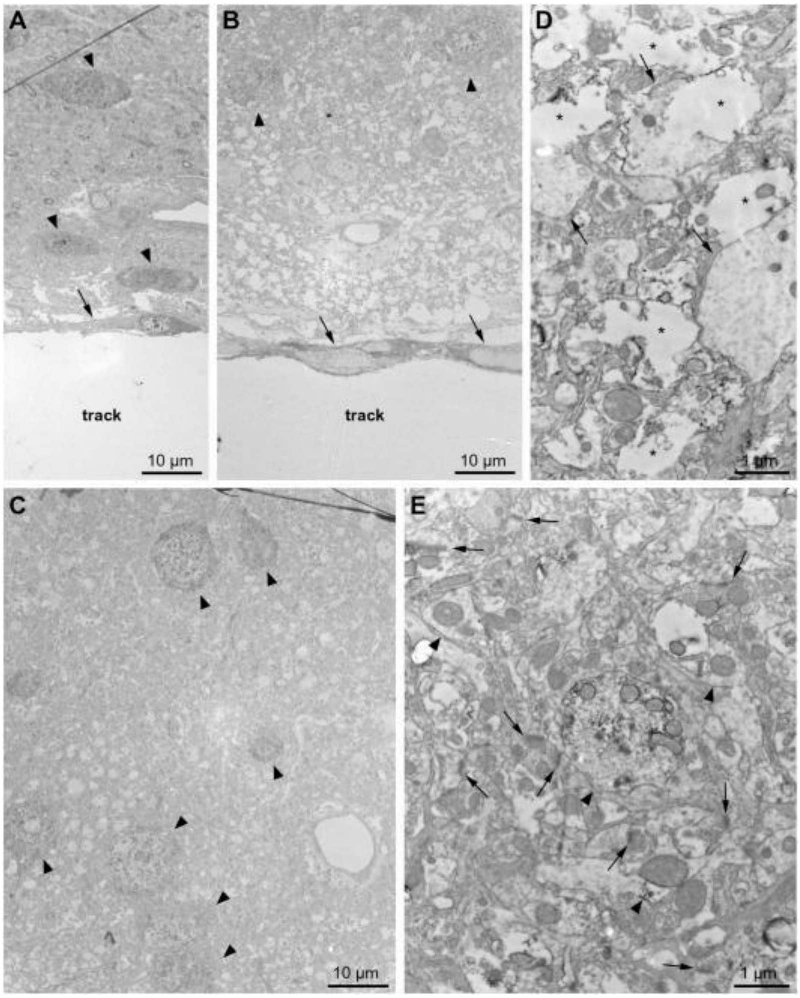

Figure 4. Electron micrographs of the neuronal tissue surrounding the SU-8 probe after chronic implantation.

A, B: The glial scar surrounding the track in 5-10 µm thickness (arrows). We have found that the damage around the probe was not uniform in the different samples and regions. **A**: shows a sample with a low amount of damage in the form of a few caverns. In this picture, neuronal cells (arrowheads) are visible as close as 10-15 µm, and the astroglial scar is less prevalent. Image **B:** shows an area with a thicker glial scar and numerous large caverns up to 20-40 µm from the track, indicating more damage. In this case, the neurones appeared around a distance of 40 µm. **C**: NeuN positive cells from a higher distance (60-145 µm). Occasionally caverns are still visible at this distance. **D**: Higher magnification image of the more damaged area in picture **B**. Arrows indicating the numerous glial elements visible. Large caverns and incomplete, damaged membranes are also visible (*). **E**: Image from 70-80 µm from the track showing a normal tissue structure with many cell bodies (arrowheads) and synapses (arrows).

4.1.5.2 Synaptic contacts in the neuropil around the probe

Preserving synaptic contacts in the tissue around the probe is essential for the extracellular recordings and for the tissue to function properly. We have measured the density of synaptic connections regarding the distance from the probe as a sign of the effects the SU8 material had on the brain tissue (Table 3). We have investigated the surrounding tissue up to a 190 µm distance. At distances lower than 5 µm, we did not see synapses (due to the glial scar), from 6-12 µm, the contacts were visible occasionally (Figure 5). At this distance (0-12 µm), the number of synaptic elements was significantly lower, at 0-12 µm, it was 6.44±13.05/100 µm^2 while at 180–192, it was 36.45±10.19/100 µm^2 ($p<0.005$) (Figure 5, Table3). Between 12-24 µm from the probe, the density was still decreased to 16.01±13.47/100 µm^2 but this decrease was not significant ($p=0.1150$). At distances from 24 µm to 192 µm, the number of synaptic elements was comparable to the control area.

Notably, close to the track (less than 30 µm distance), some synapses had shown signs of damage as incomplete membranes of the pre/post-synaptic element, but the synaptic cleft was preserved (Figures 3 and 4). We did not find any damaged synapses over 60 µm from the track.

Distance from the track (µm)	DistaNumber of synaptic contacts/ 100 µm area	StDev
0–12 *	6.44	13.05
12–24	16.01	13.47
24–36	28.74	11.47
36–48	30.06	12.13
48–60	30.02	13.12
60–72	38.84	13.00
72–84	28.74	12.17
84–96	36.47	11.49
96–108	29.95	15.43
108–120	31.20	12.83
120–132	35.79	11.01
132–144	29.76	14.10
144–156	29.80	9.75
156–168	29.90	8.56
168–180	30.70	14.03
180–192	36.45	10.19

Table 3. Changes in the synaptic density in the neuropil based on the distance of the probe.

* indicates the significant difference compared to the control region ($p<0.05$).

Fig. 5. Changes in the density of synaptic contact in the close vicinity of the probe

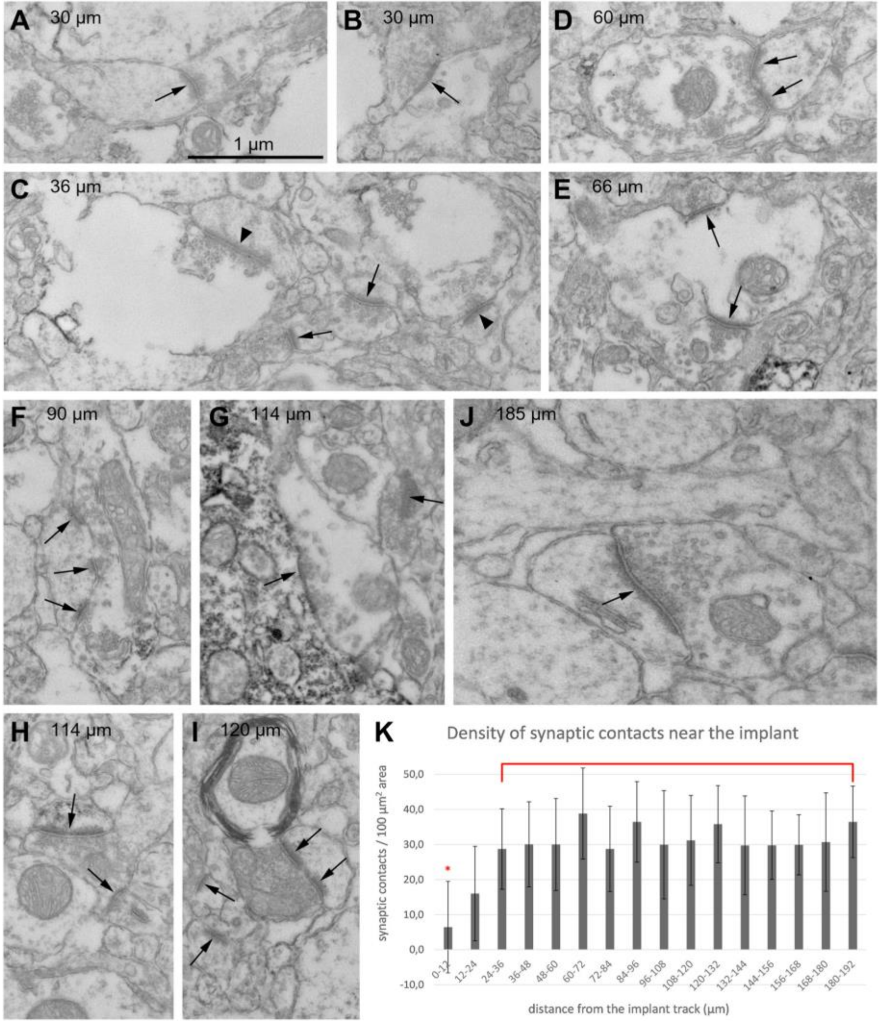

The arrows indicate the synaptic contacts in all pictures**.** The distance from the track is displayed on the images**.** In images **A-C**, it is visible that numerous synaptic contacts were present as close as 30 µm. On **C** arrowheads indicating synapses with incomplete post/presynaptic membranes, this was present mainly at close distances. Images from a greater distance (**D-I**) showing a well-preserved synaptic system **K**: Number of synaptic contacts normalised for a 100 µm^2 area. We only found a significant decrease in the first area at 0-12 µm distance (red asterisk, $p<0,05$).

4.1.5.3 Changes in the amount of glial elements around the track

We quantified the amount of glial elements in the neuropil based on the distance from the probe.

We found a significant increase up to 24 µm from the probe (Figure 6). At 0-12 µm it was more pronounced, with 0.16±0.004 µm^2 area of glial elements / µm^2 area, and 0.009±0.003 µm^2 at 12-24 µm ($p<0.05$ in both cases when compared to the control area at 160-180 µm 0.003±0.002 µm^2), between 24 µm and 180 µm the amount of glial elements were comparable (Figure 6).

Notably, even at close distances, the space taken up by glial elements was only 16% of the neuropil.

Figure 6 **Quantitative analysis of the GFAP positive elements based on the distance of the track on the electron microscopic level**

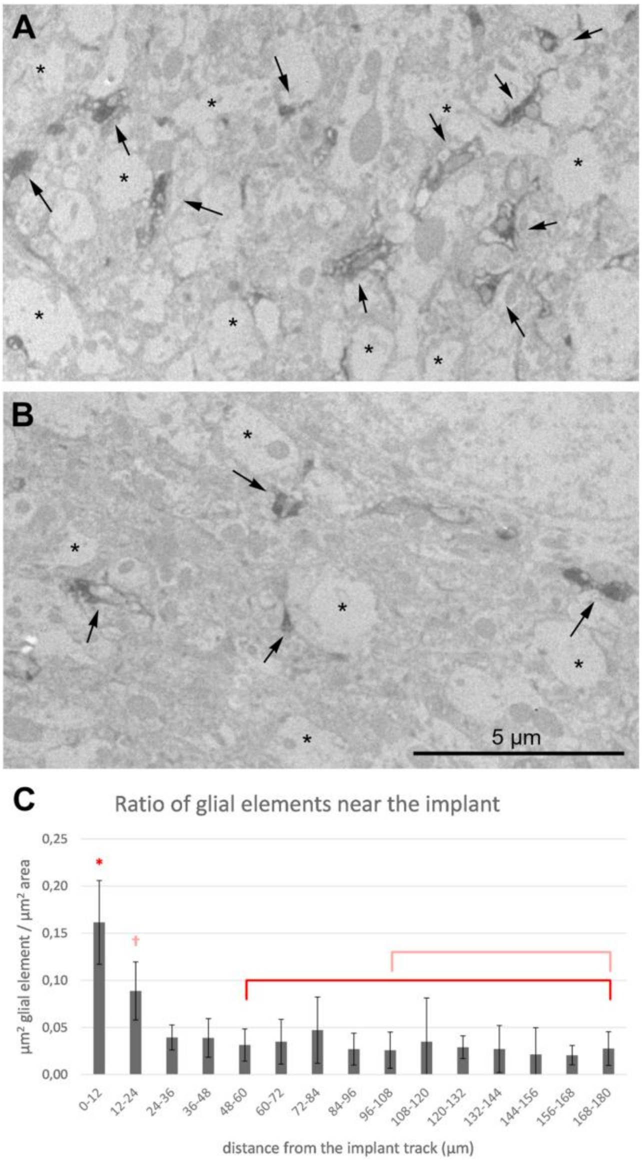

D Measurements of the amount of glial elements

Distance from the track (µm)	Rati of glial elements (µm2 glial elements/µm2 area)	StDev
0–12 *	0.16	0.04
12–24 †	0.09	0.03
24–36	0.04	0.01
36–48	0.04	0.02
48–60	0.03	0.02
60–72	0.03	0.02
72–84	0.05	0.04
84–96	0.03	0.02
96–108	0.03	0.02
108–120	0.03	0.05
120–132	0.03	0.01
132–144	0.03	0.02
144–156	0.02	0.03
156–168	0.02	0.01
168–180	0.03	0.02

A: Image from a close distance (24 µm) from the probe, numerous glial elements (arrows) and caverns (*) are visible. **B**: At a higher distance (80 µm), caverns are still visible (*), but the amount of glial elements is lower (arrows). **C**: Analyses of the space occupied by glial elements normalised for 1 µm^2 tissue area based on the distance. A red asterisk or cross shows the significantly higher glial presence at distances lower than 24 µm. Even at a close distance, the amount of glial elements was only 16%. **D**: Table presenting the measurements about the amount of glial cell elements. Significant differences are indicated by a red asterisk or cross.

4.2 Investigation of the perisomatic innervation on layer 2/3 pyramidal cells in epilepsy

4.2.1 Spontaneous Population Activities

We have investigated neocortical samples from NoEpi (12 slices from 8 patients) and ResEpi patients (8 slices from 6 patients). We have recorded SPA in ACSF as expected based on previous research (70,71,73,74) (Figure 7, Table 6).

SPA events can occur in all cortical layers. In this study, in 11 out of 12 NoEpi and 6 out of 8 ResEpi cases, we have recorded the SPA in the supragranular layers (Layers 1-3) and in the remaining cases in the granular-infragranular layers (L4-6, 1 NoEpi and 2 ResEpi slices).

The recurrence frequency of the events was 1.37 [0.74 – 1.76] Hz in NoEpi and 0.88 [0.67 – 1.84] Hz in ResEpi samples. It did not differ significantly (Welch's t-test, $p>0.05$, Table 4, Figure 7).

The LFPg amplitude was significantly higher in the ResEpi samples (Welch's t-test, $p=0.035$, Table 5), in the NoEpi cases, it was 36.30 [25.01 – 46.44] μV, and in the ResEpi it was 66.01 [36.46 – 106.49] μV.

The MUA activity was also significantly different (Welch's t-test, $p=0.035$, Table 5), it was 0.67 [0.56 – 1.10] μV in NoEpi and 3.12 [1.82 – 5.36] μV in ResEpi, the latter being significantly higher (Table7, Figure 8).

4.2.2 Perisomatic inhibition in SPA generation

In this project, we were interested in the role of perisomatic inhibitory cells in generating SPAs in the epileptic and non-epileptic neocortex. We reached this goal by applying various pharmacological agents to slices showing SPAs and then recorded the changes in the different attributes of the events. All changes are compared to data recorded in ACSF (physiological recording solution as described above) before the drug applications (or in some cases in the washing phase between the applications of different pharmacological agents), and the data recorded after the drug applications are represented as percentages of the baseline. We have washed out the pharmacological agents with ACSF to examine whether the SPAs are able to return to the recorded baseline level (Table 4,5,6,7, Figure 7,8).

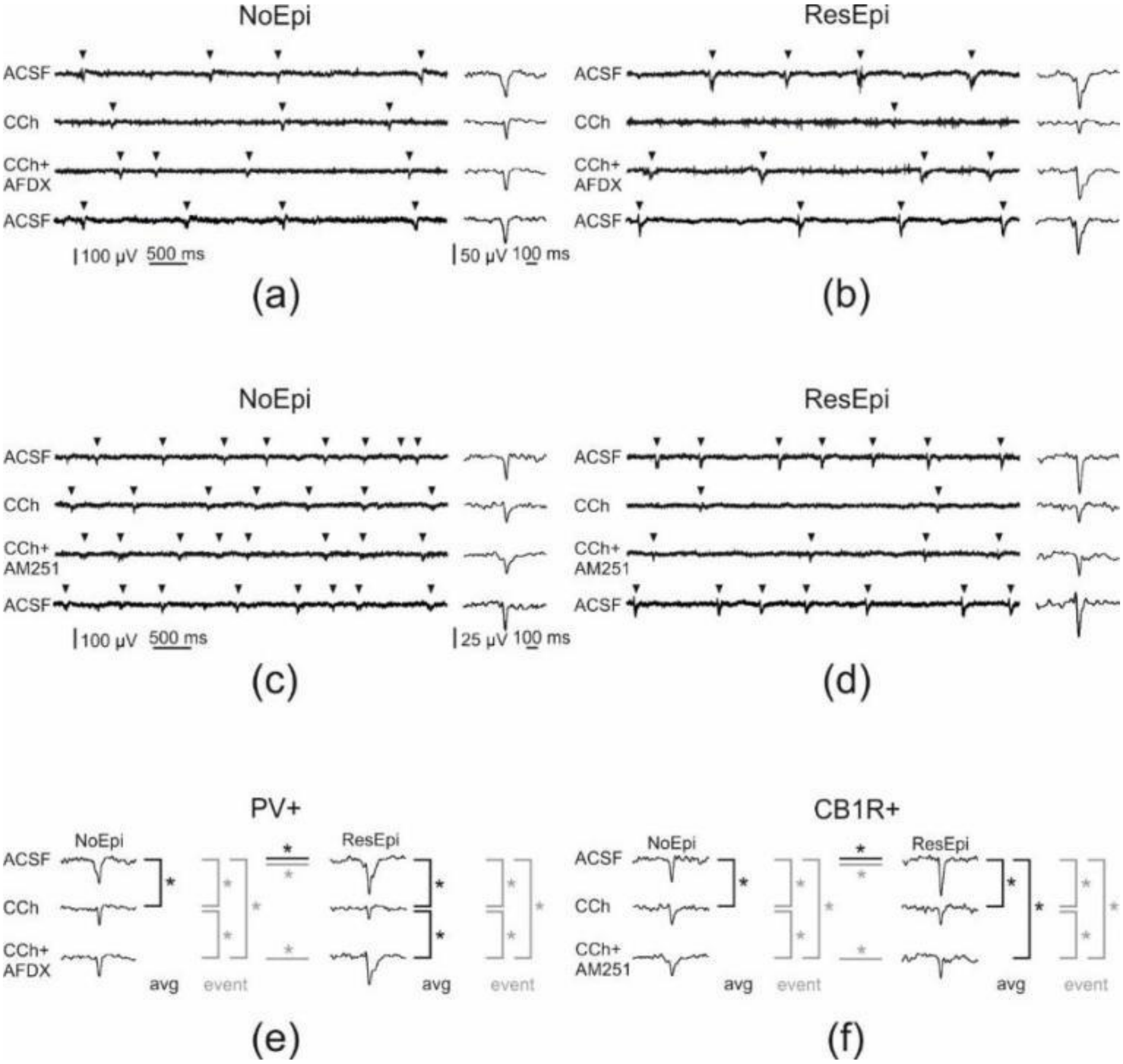

<u>Figure 7</u> In vitro pharmacological experiments regarding the SPAs in epileptic and non-epileptic human neocortical samples

Arrowheads indicate the individual SPA events. ACSF indicates control recordings and washout periods. In NoEpi cases (**a, c**) is visible that carbachol (Cch) had no effect on the recurrence frequency, but it reduced the LFPg amplitude. In ResEpi cases (**b, d**), both attributes were decreased significantly by Cch. AFDX-116 applied together with Cch partially rescued the LFPg but had no effect on the recurrence frequency in NoEpi cases (**a**). In ResEpi (**b**) cases, it restored both the LFPg amplitude and the recurrence frequency (**b**). AM-251 combined with Cch in NoEpi samples, the recurrence frequency was control-like (ACSF) while the LFPg amplitude was still reduced but higher than only in Cch. In ResEpi, we have only recorded a more minor recovery by AM-251 (**b**). We have been able to wash out the pharmacons in ACSF (**a-d** lowest line). **e, f**: Significant differences between the different agents (*) in AFDX-116(**e**) or AM-251 (**f**). Black lines indicate changes regarding the averaged LFPg, while the grey ones show the changes in the LFPg of single SPA events. Horizontal lines indicate differences between the two patient groups.

Table 4. Recurrence frequency of Spontaneous Population Activities. *: significant difference between the physiological solution and carbachol (One-way Repeated Measures ANOVA, $p<0.05$). #: significant difference between NoEpi and ResEpi (Welch’s t-test, $p<0.01$). Data are shown as median [1st – 3rd quartiles]. The Changes compared to the baseline in the physiological solution are shown as percentages of it(baseline being 100%).

Frequency (Hz)	**NoEpi**					**ResEpi**			
		Physiological solution	Pharmacological agent	Changes compared to physiological solution (%)			Physiological solution	Pharmacological agent	Changes compared to physiological solution (%)
Carbachol	n=12	1.37 [0.74 – 1.76]	1.24 [0.59 – 1.57]	80 [72 – 95]	#	n=8	0.88 [0.67 – 1.84]	0.10 [0.02 – 0.37] *	9 [3 – 27]
AF-DX 116	n=3	0.98 [0.85 – 0.99]	0.97 [0.77 – 1.02]	99 [88 – 102]		n=4	1.28 [0.99 – 1.56]	1.33 [1.15 – 1.48]	102 [99 – 107]
AF-DX 116 + Carbachol	n=6	0.99 [0.78 – 1.45]	0.82 [0.72 – 1.19]	78 [75 – 87]		n=4	1.28 [0.99 – 1.56]	0.90 [0.87 – 1.07]	83 [71 – 96]
AM-251	n=3	1.02 [0.61 – 1.21]	1.07 [0.63 – 1.18]	92 [91 – 99]		n=5	0.94 [0.81 – 1.71]	0.97 [0.93 – 1.49]	96 [94 – 115]
AM-251 + Carbachol	n=5	1.40 [1.23 – 1.51]	1.47 [1.03 – 1.50]	88 [84 – 97]		n=5	0.94 [0.81 – 1.71]	0.83 [0.02 – 0.94]	88 [2 – 93]

Table 5. Changes in the LFPg amplitudes of SPAs. *: significant difference in the averaged LFPg amplitude between physiological solution and pharmacological agent (One-way Repeated Measures ANOVA, $p<0.05$). #: significant difference between the physiological solution and pharmacological agent in case of LFPg amplitude of individual SPA events ($p<0.05$). @ significant difference in the case of LFPg amplitude of individual SPA events between carbachol and pharmacological agents ($p<0.05$). &: significant difference between carbachol and pharmacological agent in case of LFPg amplitude of individual SPA events ($p<0.01$). *: significant difference between NoEpi and ResEpi in case of averaged LFPg amplitude (Welch's t-test, $p<0.05$). #: significant difference between NoEpi and ResEpi in the case of LFPg amplitude of individual SPA events (Welch's t-test, $p<0.01$). Data are shown as median [1st – 3rd quartiles]. The Changes compared to the baseline in the physiological solution are shown as percentages of it (baseline being 100%).

LFPg amplitude (μV)	**NoEpi**					**ResEpi**			
		Physiological solution	Pharmacological agent	Changes compared to physiological solution (%)			Physiological solution	Pharmacological agent	Changes compared to physiological solution (%)
Carbachol	n=12	36.30 [25.01 – 46.44]	23.42 [20.00 – 31.01] *#	68 [63 – 77]		n=8	66.01 [36.46 – 106.49]	18.10 [12.20 – 31.21] *#	37 [25 – 45]
AF-DX 116	n=3	38.67 [27.55 – 38.75]	34.88 [25.06 – 41.60] &	93 [91 – 109]	*#	n=4	79.43 [60.50 – 95.75]	79.70 [59.51 – 96.74] &	99 [99 – 100]
AF-DX 116 + Carbachol	n=6	38.75 [38.08 – 62.72]	34.28 [28.52 – 39.61] #&	92 [75 – 96]	*#	n=4	79.43 [60.50 – 95.75]	63.87 [53.55 – 76.51] #@&	87 [83 – 91]
AM-251	n=3	35.48 [29.46 – 41.67]	29.71 [28.06 – 41.98] &	113 [98 – 113]	#	n=5	55.66 [46.00 – 89.09]	63.13 [46.15 – 88.51] &	100 [99 – 100]
AM-251 + Carbachol	n=5	39.80 [27.18 – 46.92]	22.81 [22.34 – 34.12] #&	68 [64 – 95]	#	n=5	55.66 [46.00 – 89.09]	22.78 [11.18 – 33.91] *#&	38 [34 – 50]

4.2.3 Overall perisomatic inhibition

First, we applied carbachol (Cch, NoEpi n=12, ResEpi=8 slice, Table 6) in 5 μM concentration (in ACSF) to decrease the GABA release from the perisomatic inhibitory cells (87). Since Cch is a mAChR agonist, it has a mixed effect on inhibitory and excitatory cells (126,128), but its effects are much stronger on inhibitory cells. The Cch can block the perisomatic inhibitory cells it acts on the PV-positive cells through the M2 receptor, while it has an indirect effect on the CB1R positive cells via endocannabinoid release from their postsynaptic targets by the activation of M1/M3 receptor.

In NoEpi slices, we have recorded a slight decrease in the recurrence frequency of the SPAs (1.24 [0.59 – 1.57] Hz) to 80 [72 – 95] % of the baseline, although this was non-significant. In the case of ResEpi slices, the recurrence frequency of the SPAs was significantly lower, only 9 [3 – 27] % of the baseline (0.10 [0.02 – 0.37] Hz, One-way Repeated Measures ANOVA, p=0.006). In 5 cases, the SPA reduced to below 30% of the baseline, and in two of these cases, it disappeared (Figure 7, 8, Table 4).

Table 6. Number of SPA events in the pharmacological experiments

The table shows the recorded single SPA events in each slice (each row) that we recorded.

	ACSF	Cch	ACSF	AFDX-116	AFDX-116+Cch	ACSF	AM-251	AM-251+Cch	ACSF
NoEpi	156	502	350	78	133	504	334	123	39
	171	381					204	261	314
	95	88	189	162	176				442
	184	63	191	115	106				242
	282	137			253				400
	345	705			645				494
	223	75						94	87
	437	147						193	176
	246	233						225	592
	473	553							773
ResEpi	493	473	247	330	99	545	194	126	527
	164	95	862	414	124	922	432	0	628
	558	369	235	319	299	599	723	399	185
	81	5				69	65	6	306
	247	0							673
	587	7							235
	18	0							350

Changes in the LFPg amplitude the differences were significant in both patient groups. In NoEpi cases, it has decreased to 68 [63 – 77] % (23.42 [20.00 – 31.01] µV, One-way Repeated Measures ANOVA, p=0.002). While in the ResEpi samples, it was 37 [25 – 45] % (18.10 [12.20 – 31.21] µV, One-way Repeated Measures ANOVA, p=0.004). It is visible that the changes in LFPg amplitude were more pronounced in the ResEpi samples, but this was non-significant compared to the NoEpi slices (Welch’s t-test, p>0.05) (Figure 7,8, Table 5).

We have also examined the LFPg amplitudes regarding single SPA events that changes were similar with even stronger significance in both patient groups (One-way Repeated Measures ANOVA, p <0.0001).

We have found that the MUA also decreased significantly in Cch compared to the baseline in both groups. In the NoEpi group, it was 81 [57 – 107] % (0.67 [0.46 – 0.85] µV), while in the ResEpi one, it was 43 [22 – 85] % (1.21 [0.41 – 3.03] µV, One-way Repeated Measures ANOVA, p>0.05 in both cases) (Figure7, 8, Table7).

We have been able to wash out the effects of Cch to the levels of the baseline recordings regarding all three aspects of the events, (Figure 7, 8, Table 6).

Table 7 Multy Unit Activity amplitude changes. *: significant difference between NoEpi and ResEpi (p<0.05). Data are shown as median [1st – 3rd quartiles]. The Changes compared to the baseline in the physiological solution are shown as percentages of it (baseline being 100%).

MUA amplitude (µV)	**NoEpi**					**ResEpi**			
		Physiological solution	Pharmacological agent	Changes compared to physiological solution (%)			Physiological solution	Pharmacological agent	Changes compared to physiological solution (%)
Carbachol	n=12	0.67 [0.56 – 1.10]	0.67 [0.46 – 0.85]	81 [57 – 107]		n=8	3.12 [1.82 – 5.36]	1.21 [0.41 – 3.03]	43 [22 – 85]
AF-DX 116	n=3	0.98 [0.83 – 1.10]	0.94 [0.81 – 1.22]	97 [97 – 110]	*	n=4	3.89 [3.73 – 4.41]	4.89 [4.20 – 5.57]	113 [102 – 127]
AF-DX 116 + Carbachol	n=6	1.10 [0.76 – 1.41]	0.75 [0.69 – 0.95]	88 [80 – 97]	*	n=4	3.89 [3.73 – 4.41]	4.93 [4.21 – 5.31]	111 [86 – 135]
AM-251	n=3	0.87 [0.66 – 1.04]	1.24 [0.90 – 1.99]	124 [114 – 219]		n=5	4.07 [2.84 – 5.20]	3.73 [2.89 – 4.13]	92 [88 – 102]
AM-251 + Carbachol	n=5	0.87 [0.73 – 1.20]	1.32 [1.27 – 1.49]	139 [122 – 155]		n=5	4.07 [2.84 – 5.20]	2.50 [1.50 – 4.04]	65 [64 – 88]

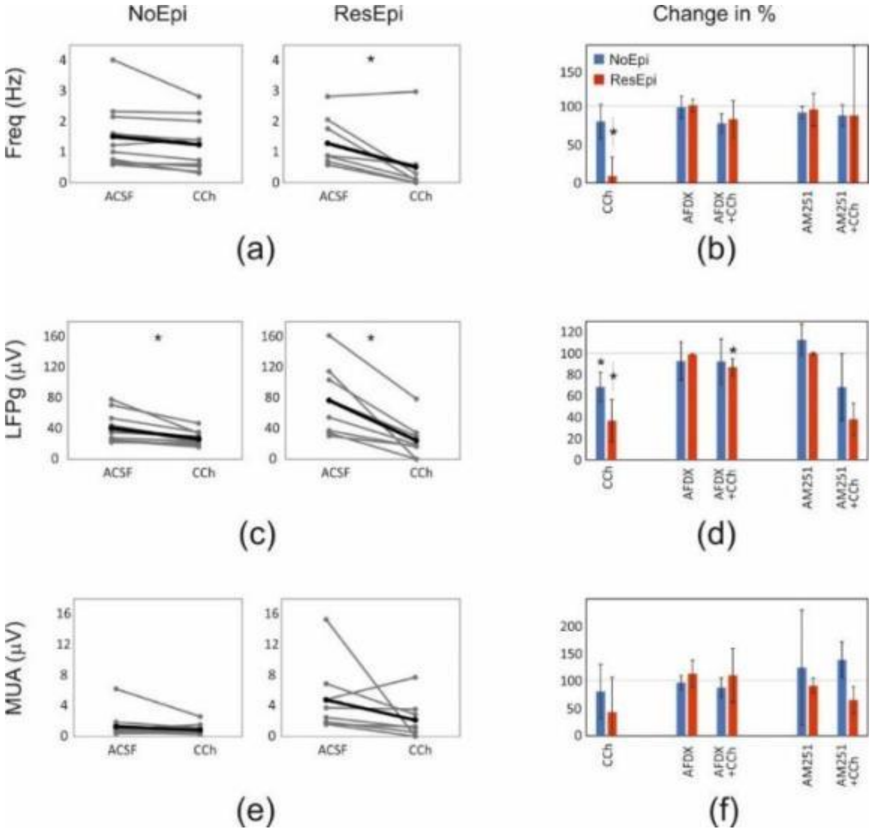

Figure 8 Statistical analysis of the pharmacological effects on the SPAs in the human neocortex

We are showing the changes in the recurrence frequency (**a, b**), the LFPg amplitude (**b**) and the MUA (**e, f**). Image a, c, and e show the differences after applying carbachol (Cch) in NoEpi and ResEpi cases. The black line is the averages, while the grey ones are the individual experiments. Images **b, d, f** show the changes caused by the AFDX-116 or AM251 application (together with Cch) on the frequency (**b**), LFPg amplitude (**d**) or the MUA (**f**). In NoEpi samples, the Cch have only reduced the LFPg amplitude (**c**). In ResEpi cases, we found a significant decrease in the frequency (**a**) and the LFPg amplitude (**c**) but not in the MUA (**e**). The measurements are shown as a percentage on b, d, and f, where 100% is the baseline experiment (ACSF). * indicates the significant differences. Cch had a more substantial effect in ResEpi than in NoEpi samples (**a, b, c, d**) both on the frequency and the LFPg amplitude. While in NoEpi cases, it only had a significant effect on the recurrence frequency (**b**).

Rescuing the PV+ neurons from Cch effects (AFDX-116 application) rescued the LFPg amplitude in ResEpi samples compared to only Cch (**d**). AM-251 can restore the activity of CB1R+ neurons, it did not cause any significant differences in the averages. (**b, d, e**)

4.2.4 Parvalbumin-positive perisomatic inhibitory cells

For the investigation of the PV-positive cells, we have used AF-DX 116 (NoEpi n=6, ResEpi n=4 slice) since these cells express the M2 type of mAChRs on their axon terminals (133,146), so blocking these should prevent the effects of Cch on them (119). We have used AF-DX 116 in 10 μM concentration combined with 5 μM Cch on 6 NoEpi and 4 Res Epi slices.

In the NoEpi group, the recurrence frequency decreased non-significantly 78 [75 – 87] % (0.90 [0.87 – 1.07] Hz, One-way Repeated Measures ANOVA, $p>0.05$), which is similar to the effect of Cch alone. In the case of the ResEpi samples, the AF-DX116 were more effective in preventing the impact of Cch 83 [71 – 96] % (0.90 [0.87 – 1.07]) compared to the baseline (One-way Repeated Measures ANOVA, $p>0.05$) (Figure 7, 8, Table 4).

We have found that the LFPg amplitudes were less affected than in applying only Cch. It was 92 [75 – 96] % (34.28 [28.52 – 39.61] μV) in the NoEpi group and 87 [83 – 91] % (63.87 [53.55 – 76.51] μV) in the ResEpi one. The effects were only significant in the case of the Res Epi group (One-way Repeated Measures ANOVA, $p=0.028$). We have also measured the changes regarding the single SPA events, and we have found that the changes were significant in both groups ($p<0.0001$) compared to the application of only Cch, but it was significantly lower than the baseline (One-way Repeated Measures ANOVA, $p <0.0001$ in both groups). The AFDX-116 applied together with Cch was able to partially rescue the SPA events (Table 5, Figure 8).

The changes in the MUA amplitude were not significant in NoEpi 88 [80 – 97] % (0.75 [0.69 – 0.95] μV) and in ResEpi 111 [86 – 135] % (4.93 [4.21 – 5.31] μV).

We have also applied the AFDX-116 without carbachol in 3-3 NoEpi and ResEpi slices. We found no significant changes (One-way Repeated Measures ANOVA, $p>0.05$, Figure 8, Table 7).

In summary, saving the Parvalbumin-positive cells from the effects of carbachol only partially restored the SPA events. The restoring effects were more pronounced in the ResEpi group, but notably, the impact of Cch is also significantly higher in the ResEpi than in the NoEpi group.

4.2.5 The role of CCK/CB1R positive interneurons

On the type one Cannabis receptor-expressing cells, the effects of Cch are indirect, because of the activation of M1/M3 mAChRs on pyramidal cells; they release endocannabinoids which are acting retrogradely on the CB1R positive cells (87,119). To prevent the effects of Cch on the CB1Rs, we have applied their selective agonist AM-251 in 1 μM concentration together with 5 μM Cch (n=5 slices both in NoEpi and ResEpi).

We have found that the recurrence frequency of SPAs in NoEpi slices remained the same as in ACSF 88 [84 – 97] % (1.47 [1.03 – 1.50] Hz). In the case of the ResEpi samples, we did not find significant changes compared to the application of Cch alone, 88 [2 – 93] % (0.83 [0.02 – 0.94] Hz) of the baseline (One-way Repeated Measures ANOVA, p>0.05, Table 4, Figures 7, 8).

The LFPg amplitudes were non significantly decreased in both patient groups (NoEpi: 68 [64 – 95] %, 22.81 [22.34 – 34.12] μV, ResEpi: 38 [34 – 50] %, 22.78 [11.18 – 33.91] μV. One-way Repeated Measures ANOVA, p>0.05). The effects were not significantly different from the Cch application alone (One-way Repeated Measures ANOVA, p>0.05) (Figures 7 and 8, Table 4). We also investigated the effects of AM-251 on the LFPg amplitude of the single SPA events, we found that it was significantly higher in both patient groups compared to the application of only Cch (One-way Repeated Measures ANOVA, p <0.0001), although the effect was still significant compared to the baseline (One-way Repeated Measures ANOVA, p <0.0001), which meant a decrease in both patient groups (Figure 7, 8, Table 5).

When we investigated the MUA amplitudes, we found no significant changes (One-way Repeated Measures ANOVA, p>0.05). In the NoEpi samples, it was 139 [122 – 155] % (1.32 [1.27 – 1.49] μV) and in the Res Epi slices, it was 65 [64 – 88] % (2.50 [1.50 – 4.04] μV).

When we applied the AM-251 on its own (NoEpi n=3, ResEpi n=5 slice), we did not find any significant changes regarding the SPAs (recurrence frequency, LFPg or MUA amplitudes, One-way Repeated Measures ANOVA, p>0.05)(Table 7).

In summary, regarding the recurrence frequency, we only found a tendency to recovery by the application of AM-251 in the ResEpi samples compared to the effects of only the

Cch. In both groups, the LFPg amplitude was partially restored. The amplitude of changes was lower than the ones caused by the application of AF-DX116 (Figures 7, 8).

4.2.6 Anatomical investigation of the perisomatic inhibitory cells

4.2.6.1 Light microscopy of the PV-positive inhibitory cells

The Ca^{2+} binding protein parvalbumin is expressed in the chandelier cells and the fast-spiking basket cells in the human neocortex (92,93). The chandelier cells target the axon initial segments on the pyramidal cells, while the fast-spiking basket cells aim at the same cells' soma (Figure 9).

We investigated 12 NoEpi and 12 ResEpi neocortical slices with parvalbumin immunostaining. The PV antibody stained non-pyramidal shaped cells in all 6 layers of the neocortex, with a significant axonal cloud around layer 3 as expected (92). In both epileptic and non-epileptic samples, the cells are presented as having multipolar cell bodies, long aspiny dendrites travelling out of the layer of the cell body (Figure 9). We found PV-positive terminal in all cortical layers, forming basket-like formation in both patient groups and the typical axo-axonic formations (not shown) were also visible in some cases, especially in the infragranular layers. The number of PV-positive cell bodies was slightly lower in the epileptic samples, as we described previously (73).

4.2.6.2 Type one cannabinoid receptor positive interneurons

The CCK/ CB1R positive interneurons are a non-overlapping perisomatic inhibitory cell type (compared to PV-positive cells) (77). In the neocortex, CB1R can only be found in symmetric (presumably inhibitory) synapses in rodents and primates (102,147).

We carried out CB1R immunostaining in samples from 9 NoEpi and 8 ResEpi patients. We have found the axonal clouds to be homogenous in both groups and in all cortical layers, which is similar to the monkey brain, as described previously (102). In the parietal cortex, we found a denser axonal cloud in layer 4, while in the temporal cortex, it was located in layers 1-2, also similar to the monkey brain (102). It is possible to find basket-like formations just like in the case of PV-positive terminals, but the CB1R-positive ones are less pronounced. We found no apparent changes in the CB1R staining between the non-epileptic and epileptic samples (Figure 9).

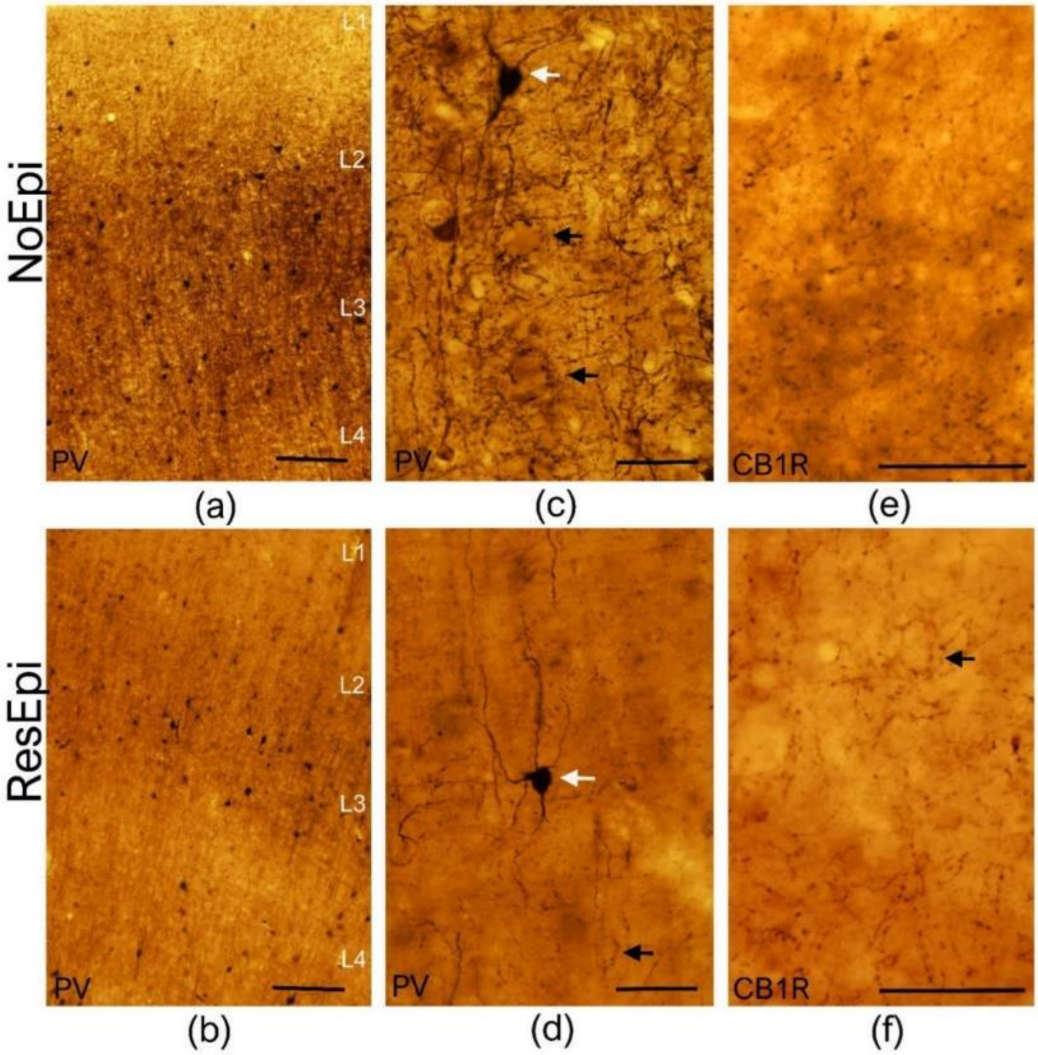

<u>Figure 9.</u> Light microscopic images of the human neocortex.
a, b: Distribution of the parvalbumin-positive cells in the supragranular and granular layers of NoEpi (**a**) and ResEpi (**b**) human cortical brain slices. It is visible that the ResEpi sample contains slightly less stained cell bodies and that a more pronounced axonal bundle is visible in layer 3. **c, d**: high magnification images of PV-stained sections from NoEpi (**c**) and ResEpi (**d**) slices. The white arrows show the PV-positive cell bodies with aspiny dendrites, while the black arrows indicate the basket-like axonal formations presumably around pyramidal cell bodies. **e, f**: CB1R positive axons in the NoEpi (**e**) and ResEpi (**f**) samples from layer 3 of the human neocortex. The black arrow shows a basket-like formation. Scale bars: **a**, **b**: 200 µm, **c-f**: 50 µm

<u>4.2.6.3 Changes in the microstructure of the perisomatic inhibitory system</u>

Since we have been able to record the SPAs most frequently from the supragranular layers, we have chosen layers 2-3 for the quantitative electron microscopic investigations.

We investigated the perisomatic synaptic innervation of the layer 2/3 human pyramidal cells, as well as the distribution of perisomatic axon terminals regarding epilepsy and the generation of SPAs. As described above, CB1R has a different distribution in different cortical areas, so we only included samples from the temporal lobe in the investigation.

We have investigated the PV- and the CB1R-stained samples separately to determine the ratio of the two groups. We were also interested in the changes related to the ability to generate synchronous activity, so we have chosen to investigate two regions of interest (ROIs) from each slice, one where we recorded SPA and one where it was not present. We have used 6 slices from both PV- and CB1-stained samples (3-3 slices NoEpi and ResEpi), investigating two ROIs in each slice (24 ROI from 12 slices). Overall, we measured the perisomatic inhibition on 123 cells from 4 NoEpi patients (13.1±4.8 somata/ROI) and 157 cells in 6 ResEpi slices (10.3±3.7 somata/ROI), including both the parvalbumin and the CB1R immunostained samples (3 NoEpi and 3 ResEpi each). We have found 297 synaptic contacts in the NoEpi and 387 in the ResEpi samples (Figure 10, 11, Table 8).

4.2.6.4 Epilepsy-related changes in the Layer 2/3 of the human neocortex

In the human hippocampus (155) and the neocortex (99), inhibitory cells are shown to participate in the epileptic reorganisation.

Our goal was to gain more information about the changes regarding the perisomatic inhibitory system in the epileptic and non-epileptic human neocortex. We examined the synaptic terminals on the somata of layer 2/3 pyramidal cells in NoEpi versus ResEpi samples, regardless of the ability to form SPAs. We have found only symmetric (presumably inhibitory) synapses terminating on the cell bodies. We calculated each pyramidal cell's synaptic coverage (µm synaptic active zone/100 µm soma perimeter). We defined the coverage as how many µm synaptic active zone would be on 100 µm soma perimeter. The overall synaptic coverage did not change, it was 1.07 [0.62 – 1.50] µm synapse/100 µm soma perimeter in NoEpi and 1.12 [0.64 – 1.67] µm synaptic active zone/100 µm soma perimeter in ResEpi (Mann-Whitney U test, p>0.05).

We found that the average length of the synaptic active zones was not significantly different when we compared the NoEpi and ResEpi samples (Kruskal-Wallis ANOVA, p>0.05). The same can be said about the region generating or lacking SPAs (Kruskal-Wallis ANOVA, p>0.05) (Table 8, Figure 12).

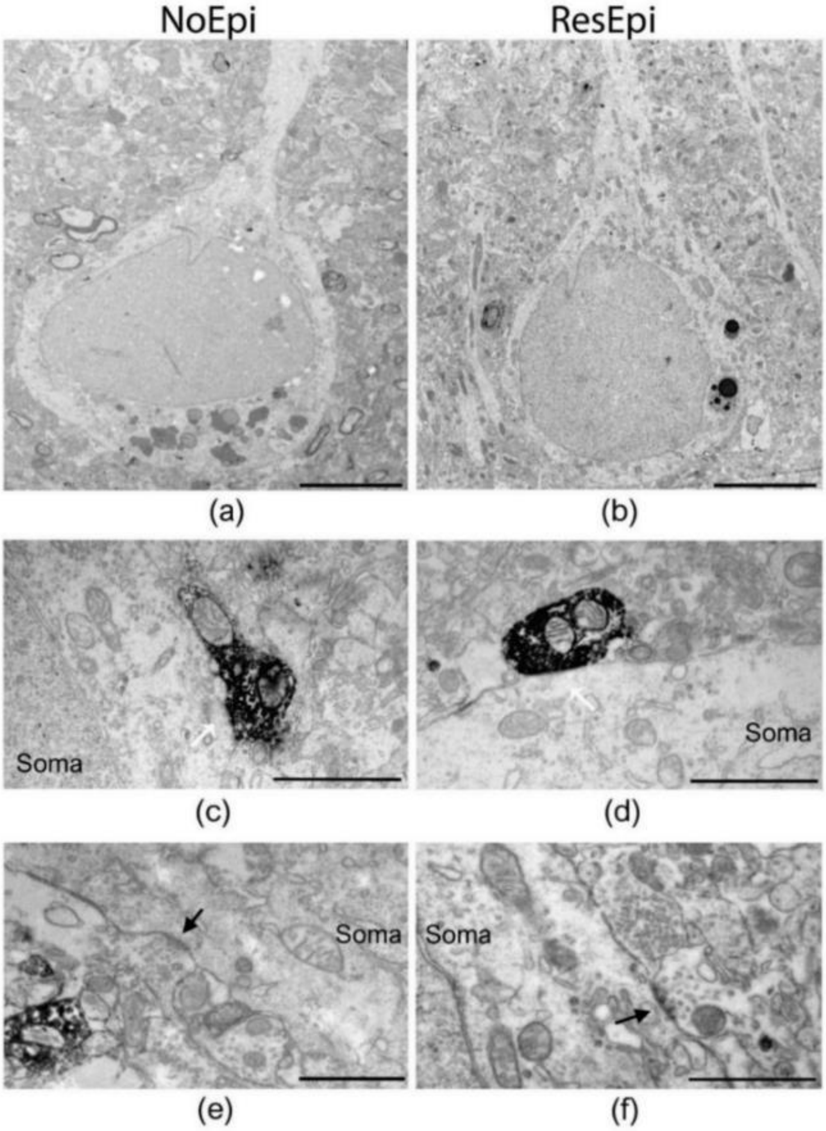

<u>Figure10.</u> Electron microscopic images of parvalbumin stained layer 2/3 human cortical pyramidal cells. All pictures are from areas which generated SPAs (**a, b**): Cell bodies of pyramidal cells from NoEpi (**a**) and ResEpi (**b**) slices. (**c, d**) PV-positive axon terminals (white arrows) from NoEpi (**c**) and ResEpi (**d**) samples. (**e, f**): Unstained synapses terminating on soma (black arrow) of NoEpi (**e**) and ResEpi (**f**) slices. All synapses were symmetric (presumably inhibitory). Scale: **a, b**: 5 μm, **c-f**: 1 μm.

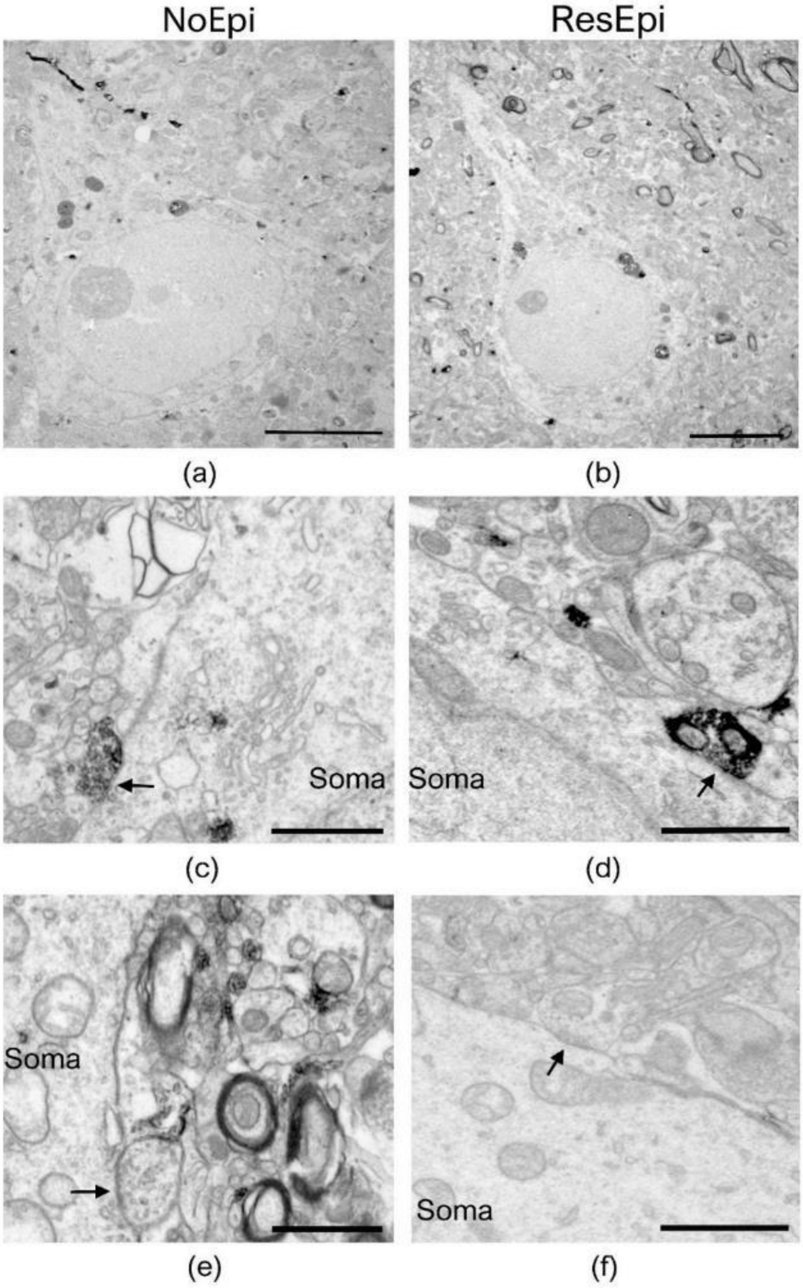

<u>Figure 11.</u> Electron micrographs of CB1R stained samples from the temporal cortex. (a, b): Low magnification images from L2/3 pyramidal cells, from non-epileptic (**a**) and epileptic (**b**) patients. On pictures **c-f** it is visible that both CB1R+ (**c, d**) and CB1R- (**e, f**) synapses are present at the cell bodies (black arrows). All synapses are symmetrical, suggesting their inhibitory nature. All the images are from regions where SPAs were present. Scale bars: (**a, b**): 5 µm, (**c–f**): 1 µm.

Table 8. Quantitative electron microscopy of the perisomatic innervation in Layer 2/3 human cortical pyramidal cells Data from the quantitative electron microscopic investigation of l2/3 human pyramidal cell bodies. We found no significant differences in the overall, or the PV+ or CB1R+ synaptic coverage between either groups (NoEpi vs ResEpi, SPA vs NoSPA). We found a significant increase in the lengths of the PV+ and CB1R– synaptic active zones in the SPA-generating regions between the NoEpi and ResEpi groups. We also found a significant decrease in the number of terminals in SPA-generating regions between the NoEpi and ResEpi groups (** $p<0.01$, * $p<0.05$).

	NoEpi			ResEpi		
	Total	SPA	No SPA	Total	SPA	No SPA
Overall synaptic coverage	1.15±0.69 1.07 [0.62 – 1.50] n=123 cells	1.17±0.59 1.07 [0.80– 1.46] n=57 cells	1.13±0.77 1.07 [0.55 – 1.52] n=66 cells	1.19±0.74 1.12 [0.64 – 1.67] n=156 cells	1.13±0.78 1.03 [0.56 – 1.51] n=81 cells	1.26±0.69 1.23 [0.69 – 1.70] n=75 cells
PV+ synaptic coverage	0.52±0.49 1.07 [0.58 – 1.52] n=62 cells	0.53±0.42 0.52 [0.36 – 0.75] n=26 cells	0.52±0.53 0.52 [0.00 – 0.90] n=36 cells	0.42±0.46 1.18 [0.57 – 1.70] n=78 cells	0.40±0.46 0.34 [0.00 – 0.68] n=42 cells	0.44±0.48 0.35 [0.00 – 0.67] n=36 cells
% of PV+ synaptic coverage	42.82±33.36 46.75 [0.00 – 58.41]	39.10±31.26 45.74 [0.00 – 52.86]	48.15±36.20 52.48 [0.00 – 75.41]	34.52±34.24 30.18 [0.00 – 54.44]	29.41±28.51 27.24 [0.00 – 53.68]	33.6±34.2 32.72 [0.00 – 58.29]
CB1R+ synaptic coverage	0.44±0.41 1.04 [0.68 – 1.46] n=61 cells	0.42±0.34 0.42 [0.00 – 0.63] n=31 cells	0.45±0.47 0.37 [0.00 – 0.68] n=30 cells	0.51±0.49 1.05 [0.65 – 1.62] n=78 cells	0.43±0.47 0.38 [0.00 – 0.58] n=39 cells	0.60±0.49 0.62 [0.30 – 0.80] n=39 cells
% of CB1R+ synaptic coverage	40.79±34.42 42.82 [0.00 – 57.28]	42.50±33.49 48.35 [0.00 – 59.98]	37.86±36.62 34.75 [0.00 – 51.16]	45.15±27.51 44.66 [22.23 – 62.72]	43.77±35.96 44.18 [0.00 – 63.62]	41.7±29.1 47.76 [31.33 – 58.73]
Average length of synaptic active zones (µm)	0.232±0.046 0.229 [0.201 – 0.260] n=325 boutons	0.226±0.042 0.225 [0.198 – 0.255] n=129 boutons	0.237±0.048 0.230 [0.201 – 0.267] n=196 boutons	0.241±0.050 0.244 [0.211 – 0.270] n=333 boutons	0.244±0.051 0.249 [0.213 – 0.274] n=188 boutons	0.237±0.048 0.237 [0.207 – 0.266] n=145 boutons
Average length of synaptic active zones of PV+ terminals	0.230±0.043 0.228 [0.200 – 0.256] n=60 boutons	0.231±0.037 ** 0.231 [0.203 – 0.253] n=25 boutons	0.229±0.047 0.228 [0.196 – 0.263] n=35 boutons	0.253±0.044 0.255 [0.228 – 0.275] n=65 boutons	0.26±0.035 ** 0.260 [0.243 – 0.276] n=36 boutons	0.245±0.051 0.244 [0.217 – 0.275] n=29 boutons
Average length of synaptic active zones of PV- terminals	0.225±0.046 0.228 [0.194 – 0.257] n=77 boutons	0.231±0.039 0.234 [0.201 – 0.258] n=40 boutons	0.219±0.052 0.212 [0.179 – 0.249] n=37 boutons	0.237±0.039 0.241 [0.212 – 0.262] n=129 boutons	0.237±0.038 0.240 [0.209 – 0.259] n=73 boutons	0.237±0.041 0.242 [0.213 – 0.264] n=56 boutons

Average length of synaptic active zones of CB1R+ terminals	0.234±0.048 0.229 [0.196 – 0.264] n=77 boutons	0.219±0.042 0.216 [0.193 – 0.255] n=26 boutons	0.242±0.049 0.241 [0.198 – 0.277] n=51 boutons	0.229±0.064 0.226 [0.193 – 0.282] n=61 boutons	0.229±0.076 0.237 [0.154 – 0.291] n=34 boutons	0.229±0.047 0.226 [0.195 – 0.253] n=27 boutons
Average length of synaptic active zones of CB1R- terminals	0.238±0.046 0.230 [0.208 – 0.263] n=109 boutons	0.224±0.050 * 0.219 [0.199 – 0.245] n=36 boutons	0.245±0.043 0.241 [0.211 – 0.276] n=73 boutons	0.247±0.055 0.248 [0.212 – 0.273] n=78 boutons	0.253±0.053 * 0.254 [0.233 – 0.276] n=45 boutons	0.238±0.057 0.226 [0.190 – 0.259] n=33 boutons
Average number of PV+ synapses/100 µm soma perimeter	2.26±2.05 2.19 [0.00 – 3.51] n=62 cells	2.41±1.86 ** 2.23 [1.36 – 3.51] n=26 cells	2.16±2.19 2.17 [0.00 – 3.48] n=36 cells	1.30±1.76 0.25 [0.00 – 2.06] n=78 cells	1.10±1.50 ** 0.23 [0.00 – 1.90] n=42 cells	1.55±2.02 1.00 [0.00 – 2.14] n=36 cells
Average of PV- synapses/100 µm soma perimeter	2.85±2.33 2.49 [1.71 – 4.09] n=62 cells	3.39±2.20 * 2.87 [2.12 – 4.41] n=26 cells	2.46±2.38 2.17 [0.00 – 2.76] n=36 cells	2.43±2.05 2.13 [0.30 – 3.81] n=78 cells	2.26±1.96 * 2.15 [0.24 – 3.81] n=42 cells	2.64±2.17 2.09 [1.21 – 3.56] n=36 cells
Average of CB1R+ synapses/100 µm soma perimeter	1.87±1.63 2.07 [0.00 – 2.80] n=61 cells	1.97±1.47 2.21 [0.00 – 3.04] n=31 cells	1.77±1.80 1.87 [0.00 – 2.47] n=30 cells	2.37±2.22 2.02 [0.00 – 3.20] n=77 cells	2.12±2.18 1.87 [0.00 – 2.63] n=38 boutons	2.62±2.26 2.09 [1.41 – 3.64] n=39 cells
Average number of CB1R- synapses/100 µm soma perimeter	3.09±2.42 2.62 [2.03 – 4.23] n=61 cells	2.92±2.47 2.47 [1.89 – 3.95] n=31 cells	3.27±2.39 3.62 [2.07 – 4.42] n=30 cells	2.91±1.94 2.65 [1.80 – 4.53] n=77 cells	2.84±2.12 2.55 [1.31 – 4.95] n=38 boutons	2.98±1.77 2.82 [1.94 – 4.53] n=39 cells

4.2.6.5 Changes in the different perisomatic axonal inhibitions

The proportion of PV-positive terminals in NoEpi samples was 46.75 [0.00 – 58.41] % and 30.18 [0.00 – 54.44] % in ResEpi (we handled the data from the cells separately from each patient), it did not differ significantly (Chi-square test p>0.05). In the case of CB1R staining, the ratio between stained and unstained boutons was 42.82 [0.22 – 57.28] % in NoEpi and 44.66 [22.23 – 62.72] % in ResEpi slices, also no significant changes (Chi-square test p>0.05) (Figure 12).

In NoEpi and ResEpi samples and ROIs generating or lacking SPAs, the perisomatic synaptic coverage from PV+ or CB1R+ terminals was similar (Kruskal-Wallis ANOVA, p>0.05) (Figure 12).

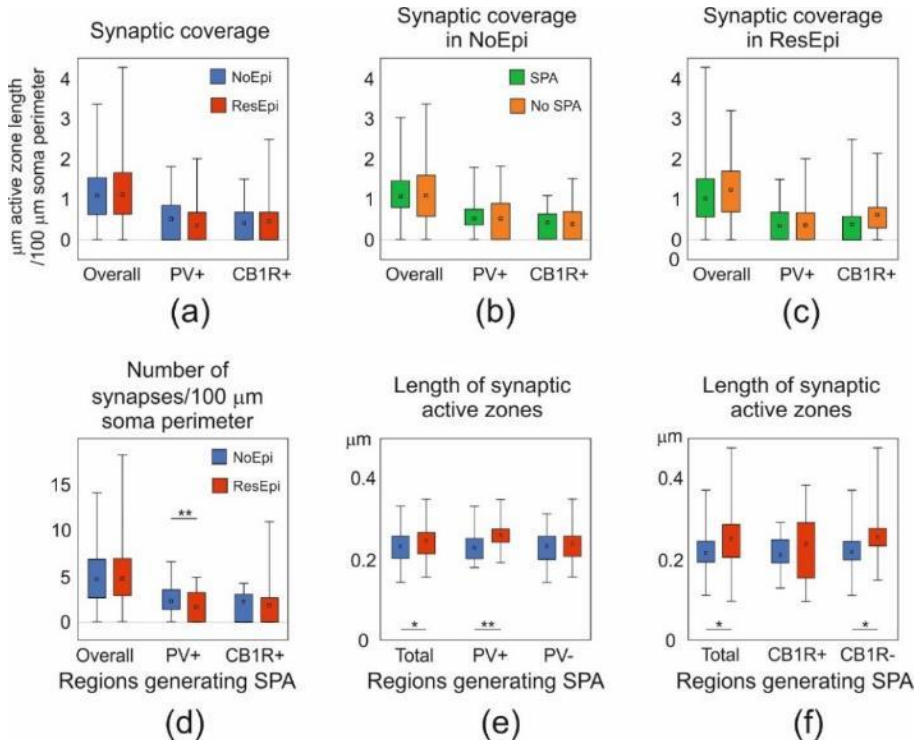

Figure 12. Changes in the perisomatic coverage of the L2/3 pyramidal cells in the human epileptic and non-epileptic neocortex

(**a,b,c**): There were no statistical differences in most of the investigated attributes. The synaptic coverage both in the PV and the CB1R immunostained samples remained unchanged. We compared the NoEpi group to the ResEpi and also the SPA-generating regions to the NoSPA regions. (**d**): In the ResEpi samples, we found a significant decrease in the number of PV+ axon terminals in the regions generating SPA (but not in the NoSPA ones). (**e,f**): In accordance with the decrease in the number, we found a significant increase in the length of the PV+ synaptic active zones, and in the CB1R- ones (these can be presumed to be PV+ ones) * p<0.05, ** p<0.01

4.2.6.6 Differences in the regions generating SPA and not generating SPA

We found no significant differences in the overall synaptic coverage regarding the ability to generate SPAs (NoEpi and ResEpi analysed separately, Kruskal-Wallis ANOVA on Ranks, $p>0.05$), SPA (NoEpi: 1.07 [0.80 – 1.46], ResEpi: 1.03 [0.56 – 1.51]) and NoSPA (NoEpi: 1.07 [0.55 – 1.52], ResEpi: 1.23 [0.69 – 1.70) (Figure 12).

We analysed the length of the synaptic active zones. We found that in regions generating SPAs, the PV-positive active zones were significantly longer in the ResEpi compared to the NoEpi slices (NoEpi: 0.231±0.037, 0.23 [0.20 – 0.25], ResEpi: 0.26±0.035, 0.26 [0.24 – 0.27], Student's t-test $p=0{,}01$). We found that the non-stained terminals in the CB1R stained tissue were also significantly longer in the epileptic tissue (NoEpi: 0.224±0.050, 0.22 [0.20 – 0.25], ResEpi: 0.253±0.053, 0.25 [0.23 – 0.28], Student's t-test $p=0.05$) in the ROIs where SPAs were present. This data suggests that since the synaptic coverage was not changed as described above, the number of synapses given by PV-positive terminals might be lower. We did find a significant difference in the number of PV+ terminals/100 µm soma perimeter between NoEpi and ResEpi slices in the region generating SPA (NoEpi: [1.36 – 3.51], ResEpi: [0.00 – 1.90], Mann-Whitney U test $p=0.01$, Figure 12).

5. Discussion

In both of our studies, we aimed to gain new information that can be utilised in investigating and treating human brain diseases, and might also can be utilised in animal research.

Investigating alternative materials for manufacturing microelectrodes that can be utilised in both acute and chronic in vivo research and for clinical application is of great importance for the improved preservation of the neuronal tissue resulting in the prolonged use of these devices.

Using human brain samples can help us better understand both the physiological and pathological processes of the human brain. While also can be an essential step in translating findings from animal models to human counterparts.

In both of our studies, we utilised electron microscopic investigations to gain a more profound understanding of the processes behind the phenomenon that can occur in rodent and human brains.

5.1 Biocompatibility of the SU8 material

We tried to better understand the biocompatibility of the SU8 material in the central nervous system (CNS). We used a large sample size and quantitative electron microscopy as a way to reach meaningful conclusions about this material. We investigated our samples in both light and electron microscopic levels to determine the level of damage caused by our probes. We measured the decrease in the number of neurons and their synapses- since their preservation is crucial to have a solid, stable signal with extracellular electrodes. We were also interested in the changes in the glial cells and their activation and scar formation around the track since astrogliosis can limit the quality of the recordings by forming a barrier between the electrode and the targeted neuronal population.

In the later years, SU-8 was used in numerous studies as a material to form implants for the central nervous system (20,28,33,41) a specific targeted profound biocompatibility study was lacking so far. Proving the safe and stable use of electrode materials in animal models before their usage in human patients is crucial for this, we need to gain knowledge about the interplay between the brain tissue end the material in question.

The success of a chronically implanted electrode can be affected by mechanical damage, such as the insertion or the motions due to the softness of the tissue, and immune reactions to the foreign object, causing inflammation and scarring (21,22). The SU-8 material already proved to be stiff enough for implantation but flexible enough to move with the neuronal tissue and not cause further damage (28,40,148). The cytotoxicity of a material can be tested in vitro with cultured cells. Intracellular measurements from neuronal cell cultures proved that SU-8 is not toxic to neurons (149). In vivo, the material has also been deemed non-toxic in the muscle (10,29,30) and, in some cases in the brain (34,40,41), but in some cases, some alterations in gene expression were shown around the electrode (150).

In our study, we showed the changes in the ultrastructure of neuronal tissue caused by the chronic implantation of SU-8 probes, showing that the material has a great biocompatibility that can be utilised in chronic implantation into neuronal tissue (151–153).

5.1.2 Neuronal survival neighbouring SU-8 implants

The inability to maintain chronic recordings over extended time periods is a widely occurring phenomenon (19,154–156). It has been established that this issue primarily stems from the chronic inflammation caused by the continuous presence of the device, leading to the degeneration and loss of nearby neurones, synapses and the formation of a glial scar around the electrode (157–159). It has been demonstrated through simultaneous intra- and extracellular recordings of individual neurons that the most effective separation of distinct units occurs when neurons are located within a radius of 50 µm around the electrode contacts (23), and the neuronal activity can be detected up to an 80 µm distance (24). Consequently, the preservation of neurons in this area is crucial for successful applications.

In this project, we investigated the long-term changes of neuronal and astroglial cells in close proximity to the SU-8 probe. We observed a significant cellular loss only within a 20 µm radius around the penetration track. Between 20 µm and 40 µm, 74% of neurons were preserved and beyond 40 µm, the neuronal density resembled the one in the control areas. With quantitative electron microscopy, we revealed the presence of synaptic contacts as close as 6-12 µm from the track, and the density of synapses returned to normal levels over 24 µm from the probe.

The high-level preservation of neurons and synaptic contacts observed in our study suggests that SU-8 is suitable for maintaining stable long-term recordings from neurons in vivo.

5.1.3. Changes in the astroglia cells surrounding the SU-8 probe

With chronic electrodes, the encapsulation -formation of a glial scar around the electrode- is known to be able to isolate the probe from the surrounding neurons, creating a seal while also increasing the distance between the targets and the electrode contacts (4,21,145,156,160,161). Although not as significantly as the neuronal cell loss, the formation of the glial scar also contributes to the long-term decline in the recording performance of the implanted devices by increasing the electrical impedance (158,162–164). It is also important to consider that glial processes, in addition to their passive barrier effect on tissue-device communication (shielding effects), also play an active role in modulating neuronal excitability, synaptic transmission, and network activity (145).

Therefore, examining the astroglial reaction at both light and electron microscopic levels is crucial when assessing the long-term functionality of an implanted device (161). In the case of our SU-8 probes, we discovered the presence of a scar approximately 5-10 µm in thickness around the track. This finding aligns with existing literature, which rarely reports a glial scar exceeding 10-20 µm from the foreign body (17,161,165).

In the light microscopic investigations, we observed a significantly increased astroglial staining in close proximity to the probe track, with a normalised pixel intensity of 0.29±0.14 compared to 1.01±0.03 in the control region. However, upon the ultrastructural examination, we found that the astroglial processes were sparsely dispersed, occupying only 16% of the neuropil within the immediate vicinity of the implant (0-12 µm). At longer distances, the ratio of glial elements was less than 5%. The disparity between the light and electron microscopic results can be attributed to methodological procedures. Namely, the penetration of immunohistochemical reagents into the brain tissue is the strongest on the surface of the sample and decreases towards the middle of the slice. The borders of the track form perpendicular surfaces inside the sample, providing an additional source of the reagent. As a result, the background staining appears darker than in regions lacking this additional surface, indicating that the considerable increase in astroglial staining observed under the light microscope is partially due to this methodological issue.

Our electron microscopic analysis revealed signs of slight gliosis around the probe, similar to the low levels observed in the vicinity of highly biocompatible silicon-based electrodes (17). This minimal encapsulation and sparse distribution of glial processes around the device may not cause a significant shielding effect. Several articles support this notion by examining the impact of glial encapsulation on recording quality through electrophysiological recordings and post hoc histological examination of the same samples. Studies investigating the relationship between recording quality and histology have demonstrated a negative correlation between astroglial density and signal quality in the case of silicon probes (22,166). It has been shown that action potential amplitudes depend on astroglial density within an 80 μm distance from the recording sites (167). The biocompatibility of polyamide probes was investigated by regular recording to follow temporal changes in various electrophysiological features (4). Stable single- and multiunit activity was recorded for several weeks with the implanted depth probes, and after a 13-week survival period, a mild to moderate tissue reaction was observed around the electrode track. Based on our results and the studies mentioned above, we can assume that the SU-8 device’s recording capability may lead to high-quality recordings even in long-term applications.

Light microscopic examination revealed a significantly elevated intensity of astroglia staining up to a distance of 480-560 μm from the device interface. Previous studies- including our own- have reported similar results with silicon and other structured materials (17,157,160).

These results suggest that the amount of the glial scar may primarily depend on the mechanical damage and less so on the electrode material or surface properties (17,160).

Our finding that the extent of the astroglial scar was more pronounced in the superficial layers of the neocortex, both in intensity and extension and gradually declining in the deeper layers, can also suggest the hypothesis mentioned earlier. The denser vascularisation of the upper layers (both in amount and size of blood vessels) might also contribute to the damage (17,168) since there will be a higher chance of the vessels getting damaged in these areas during insertion. The disruption of the blood-brain barrier is also known to contribute to the formation of a glial scar, and it is more likely to happen in the upper layers (145).

5.1.4. Biocompatibility comparison of silicon-based and SU-8 probes

Numerous studies have demonstrated the high biocompatibility of silicon-based probes in long-term in vivo applications (17,157,160,169). Hence, we sought to compare our findings with biocompatibility studies involving silicon electrodes. Our results reveal that the SU-8 probes exhibit a similarly favourable biocompatible nature in chronic implantations, as demonstrated by silicon probes.

The thickness of the glial scar and the extent of astroglial activation were comparable between the two materials (37,157,160,161,165). Likewise, the presence of glial processes in the vicinity of the probe was minimal for both materials (17,170). The preservation of synaptic contacts showed similar positive outcomes as observed with silicon-based probes (17,161). Biocompatibility studies focusing on silicon electrodes have shown a decrease in neuronal survival typically within a range of 50-200 μm (17,157,160) from the device, with rarely any preserved contact and neuron closer than 50 μm (169). In contrast, our results indicate a control-like neuronal density at 40-60 μm from the track, suggesting that the SU-8 material promotes better neuronal survival in close proximity to the implanted probe.

This observation can be partially explained by the favourable surface chemistry parameters caused by the more flexible nature of the Su-8 material compared to silicon, allowing for improved mechanical coupling with the soft brain tissue (13,14,40). It has been shown that with a platinum-based flexible probe, after an 18-week implantation, the tissue showed signs of normalisation after a period of inflammation (171), this might can be applied to the flexible SU-8-based probes too. Due to these factors, SU-8-based electrodes hold promise for developing clinically adaptable devices for human patients.

5.2 The involvement of the perisomatic inhibitory system in the formation of SPAs in epilepsy

5.2.1 Perisomatic inhibition in the formation of SPAs

In this study, we have been investigating the generation of spontaneous population activities in epileptic and non-epileptic human brain samples. Based on our previous studies, we continued to explore the presumably physiological population activity that can be generated in both the epileptic and the non-epileptic human brain in vitro, unlike the pathology-related interictal discharges (67,73). Based on our earlier findings, we discovered that excitatory and inhibitory cells participate in these events. We aimed to highlight how the perisomatic inhibitory cells participate in these events and how they change regarding epilepsy.

5.2.2 Perisomatic inhibitory cells in epilepsy

In accordance with our previous findings (73), the LFPg and the MUA amplitudes of SPA events were higher in the epileptic samples compared to the non-epileptic ones, in the physiological solution. In a bath solution containing carbachol (muscarinic agonist), the LFPg amplitude decreased in both groups, and the change was more prevalent in the epileptic tissue. In the epileptic samples, the recurrence frequency was also reduced.

We studied the participation of perisomatic inhibitory cells by selectively preventing the effects of Cch on two distinct types of perisomatic inhibitory cells. For the Parvalbumin-positive cells, we added AFDX-116, and to target the CCK/CB1R positive interneurons, we utilised AM-251.

When we excluded the PV-positive cells from the effects of Cch, we found that the LFPg decreased less strongly in the epileptic than in the non-epileptic tissue (were higher than in only Cch). Meanwhile, preventing the effect on the CB1R-positive cells, the restoring effects were similar in the two patient groups.

The larger LFPg and MUA amplitudes during the baseline activity and the more considerable effect of Cch in the epileptic tissue support the theory that more cells participate in generating the events in these samples. Epileptic hyperexcitability could explain this phenomenon. Earlier theories suggested that the loss of perisomatic inhibition (172,173) could be a possible cause of epileptic activities, but they were contradicted by further research (97,174). Our findings also show that perisomatic inhibition is preserved in the epileptic human neocortex, despite the lower number of PV-positive cell bodies (73). One reason for the reduced PV-positive cells can be that the conformation of the parvalbumin protein changes when it is bound to a high amount of Ca^{2+} ions (175,176), therefore inhibiting the antibody from recognising it and reducing the immunoreactivity, it has also been shown that there is a short term reversible decrease in the PV immunoreactivity of cells after ischemic brain damage (177). To neutralise this caveat, we investigated the CCK/CB1R positive perisomatic interneuron group too, since these are two distinct cell types. Therefore, when we carried out a CB1R staining, the unlabelled perisomatic terminals can be presumed to be parvalbumin ones.

Based on our electron microscopic investigations overall, the PV-positive and the CB1R-positive synaptic coverage and the ratio of PV+ /CB1R+ innervation were comparable in the epileptic and non-epileptic tissue. The only significant differences were the longer PV+ synaptic active zones and the lower number of these synapses in the epileptic samples in the SPA-generating areas. This finding suggests that although the PV+ synaptic coverage did not decrease, there is a change in the PV+ inhibitory system. Since the PV+ basket cells are the fast-spiking ones (77), they have an essential role in the formation of populational activities and the excitability of the system, so even small changes like the one that we described can cause an imbalance in the inhibition. The less in number but longer synaptic active zones might suggest that there could be a slight decrease in the number of PV+ cells giving the innervation, and the remaining ones are trying to rescue the function.

The data also suggest that the layer 2/3 perisomatic innervation is mainly unchanged in the epileptic tissue, just like the number of inhibitory axons in the neuropil of the same area (73).

In a previous study (100), a decreased number of inhibitory synapses were described on the axon initial segment and the soma of the peritumoral tissue from an epileptic patient. This study used only one patient who had both a tumour and epilepsy. In our electron microscopic investigations, we used one patient with both a tumour (distance from the tumour >5 cm) and epilepsy and five with only epilepsy. Furthermore, they compared the epileptic region to a ‘non-epileptic’ one from the same patient, while our controls were tumour patients with no history of epilepsy. The differences in the sampling method can explain the different outcomes.

The most common type of drug-resistant epilepsy in adult patients is medial temporal lobe epilepsy (178,179). Since the hippocampus is largely affected and often is the seizure onset zone, many patients are undergoing hippocampectomy surgeries and this removed tissue was thoroughly investigated by many research groups in the last decades. Different excitatory and inhibitory cells can both react and participate differently in epileptic activities (178), further enforcing the idea that it is essential to investigate different brain regions in epilepsy (like hippocampus vs. cortex, seizure onset zone vs. outside of it) to gain a more comprehensive idea of the background of this disease.

On layer 2/3 of neocortical pyramidal cells, the perisomatic inhibition was largely preserved, contradicting some findings in the dentate gyrus of the hippocampus (180). On the granule cells in the DG, the perisomatic input was largely increased, and the CB1R+ boutons were enhanced (180), while the PV+ ones showed a decrease both in the ratio of the synapses and the number of cells (96). In the Cornu Ammonis region of the epileptic hippocampus, as long as the pyramidal cells survive, the PV+ perisomatic innervation remains intact (94,95). In the case of the CB1R+ cells in the CA1 region, the number of boutons increased (97), and the cells could be observed even in the sclerotic tissues (103).

Our findings show more similarities to the changes in the CA than those on the granule cell layer. It is important to note that the hippocampal and the cortical pyramidal cells belong to different subgroups based on their gene expression (181,182), neurochemical identity and synaptic input-output features (79). But they are still showing more common features with the cortical pyramidal cells than the granule cells (183).

In conclusion, we found less pronounced changes in the epileptic neocortex than what can be observed in the epileptic hippocampus (178). The differences in the sustainability of the different neuronal subtypes can explain this, along with the fact that the hippocampus is the seizure onset zone in the majority of pharmacoresistant TLE patients (178). More profound changes are expected to occur in the site where the seizures originate than in the ones where it is only penetrating into. Our samples included in the quantitative electron microscopic studies were from outside the seizure focus and were only recruited during seizures.

5.2.3 The role of perisomatic inhibition in synchrony generation

Understanding the initiation of the synchronised neuronal activities is essential to understand their mechanisms and function further and explaining the differences in the physiological (SPA, sharp-wave ripple) and pathological (IID) activities.

Perisomatic inhibition is the most effective in controlling the output of the targeted cells-and to control larger neuron populations as described in the hippocampus in the case of sharp-wave ripples (68,184) and IIDs (90). In the human neocortex, inhibitory cells were described to fire at the start of both spontaneous (71) and induced (66) pathological synchronies. Based on this, it could be a possible hypothesis that these cells also control- at least partially- the spontaneous synchronisation too (like SPAs), but our study did not find a strong sign that it would be the case.

5.2.4 Involvement of the cholinergic input on pyramidal cells in epilepsy

Our approach of using carbachol to modify the muscarinic receptors is not selective to the inhibitory cells, it also affects the excitatory cells. In a healthy rodent brain, the activation of M1-type mAChRs temporarily inhibits neocortical pyramidal cells (113), followed by a prolonged voltage-dependent excitation (114). When pyramidal cells are depolarised and exhibit continuous firing, the inhibitory effect of mAChR activation becomes more robust and more reliable than when cells are at a resting membrane potential (114). During epilepsy, the increased neuronal excitability (73,114,185) can lead to sustained depolarisation of a large number of cells, resulting in a higher number of neurons firing during the SPAs. Consequently, this voltage-dependent effect can potentially explain why Carbachol may reduce the activity of more cells in the epileptic tissue, leading to a decrease in the initially higher LFPg amplitude to the same level as non-epileptic tissue. Additionally, it can substantially reduce the frequency of the recurrence frequency to a significantly lower level than in non-epileptic tissue.

6. Conclusions

Conducting studies on the long-term viability of implanted devices is crucial for both basic research purposes and future clinical applications. In this study, we focused on investigating the chronic in vivo biocompatibility of SU-8 implants in the CNS and obtained quantitative electron microscopic data with a large sample size. Achieving good electrical signals relies on biocompatibility within a 50µm radius around the recording surface (23). Notably, we observed good preservation of neurons as close as 20-40 µm from the SU-8 devices, and the density of synapses returned to control levels as close as 24 µm from the track. These findings indicate that the SU-8 material has the potential to facilitate the generation of reliable neuronal signals.

Furthermore, through electron microscopic examination, we discovered that the glial scar thickness ranged between 5-10 µm and the presence of glial cells in the neuropil did not exceed 16% in close proximity to the probe (0-12 µm), decreasing to less than 5% beyond 24 µm from the probe.

In line with previous studies conducted in cell culture models (11,32), as well as muscle (11) and subcutaneous implantations (18,39), our results demonstrate the biocompatibility of SU-8 in the CNS. However, it is crucial to reduce neurovascular damage by improving the surgical procedure (186).

Considering the low-cost fabrication and more flexible nature of SU-8-based electrodes, they hold a potential as an alternative to highly biocompatible and widely used silicon probes in future clinical and research applications.

In our human research, based on our previous findings (66,73), we formed a hypothesis, namely that the perisomatic innervation of the layer 2/3 neocortical pyramidal cells participate in the formation of spontaneous populational activities. We investigated our hypothesis on two levels. In vitro extracellular electrophysiological measurements and pharmacological modulation followed by an anatomical investigation, including quantitative electron microscopy.

Our data shows that rescuing the PV+ or the CB1R+ perisomatic inhibitory cells both at least partially restored the SPA from the effects of Cch, both in epileptic and non-epileptic samples (LFPg amplitudes in ACSF > in Cch + AFDX-116/AM-251 > in Cch). Notably, when we compared the averages rescuing the PV-positive cells only had a significant elevating effect on the LFPg amplitude in the epileptic samples. This change is further emphasised by the fact that the only significant difference that we found was in the epileptic patients in the SPA-generating ROIs, was that the PV-positive synaptic active zones were significantly increased in length and lower in number on the pyramidal cell somas. The longer synapses are associated with a stronger transmitter release and, consequently, higher synaptic strengths (187). The modified synapses can be more efficient in inhibiting their targets, therefore making certain areas more susceptible to generating synchronous events.

In our previous studies, we described that both excitatory and inhibitory cells participate in the initiation of hypersynchronous events, both spontaneous (SPA, (73) and induced (IID, (66)) cases. Possibly the more substantial effect of carbachol in the epileptic samples can be an effect throughout the excitatory cell activation, which further supports that both excitatory and inhibitory cells are required for the generation of SPAs (66).

Therefore, we suggest that the spontaneous population activities in vitro in the human neocortex can result from a complex interplay between various cell types, one of which is the perisomatic inhibitory cells.

7. Summary

In this dissertation, I wrote about how we utilised both in vivo animal studies and in vitro human brain samples to gain knowledge that can be used for better understanding, investigation and maybe treatment of human diseases like epilepsy.

In the animal studies, I carried out quantitative electron microscopy to get a detailed picture of the changes caused by chronic implantation of a SU-8-based device in the rat brain. We found good neuronal preservation as close as 20-40 μm from the SU-8 devices, and the density of synapses returned to control levels around 24 μm from the track. These findings indicate that the SU-8 material has the potential to facilitate the generation of reliable neuronal signals.

We discovered that the glial scar thickness ranged between 5-10 μm and the presence of glial cells in the neuropil did not exceed 16% in close proximity to the probe (0-12 μm), decreasing to less than 5% beyond 24 μm from the probe.

Since the material showed excellent biocompatibility, we can assume that it could be utilised in chronic applications both in animal models and after adequate testing in human patients.

We utilised in vitro electrophysiological and post hoc anatomical examinations to investigate the role of perisomatic inhibition in the formation of SPA events in the human epileptic end non-epileptic neocortex.

The pharmacological modulation of two distinct types of perisomatic inhibitory (PV or CCK/CB1R) cells showed that these cells do participate in the formation of SPAs.

In our quantitative electron microscopic investigations, we did not find a significant difference in the overall synaptic coverage on layer 2/3 pyramidal cells of the PV+/ CB1R+ coverage either. The only significant difference that we found was that in the areas of the ResEpi samples where we could record SPAs, the number of PV+ terminals was lower, while the lengths of the PV+ synaptic active zones were longer.

Based on our findings, we suggest that the spontaneous populational activities in vitro in the human neocortex can result from a complex interplay between various cell types, including the perisomatic inhibitory cells.

8. References

1. Fiáth R, Raducanu BC, Musa S, Andrei A, Lopez CM, van Hoof C, Ruther P, Aarts A, Horváth D, Ulbert I. A silicon-based neural probe with densely-packed low-impedance titanium nitride microelectrodes for ultrahigh-resolution in vivo recordings. Biosens Bioelectron. 2018;106:86–92.
2. Schwartz AB, Cui XT, Weber DJJ, Moran DW. Brain-Controlled Interfaces: Movement Restoration with Neural Prosthetics. Neuron 2006 Oct 5;52(1):205-20
3. Fiáth R, Raducanu BC, Musa S, Andrei A, Lopez CM, Welkenhuysen M, Ruther P, Aarts A, Ulbert I. Fine-scale mapping of cortical laminar activity during sleep slow oscillations using high-density linear silicon probes. J Neurosci Methods. 2019;316:58–70.
4. Fiáth R, Hofer KT, Csikós V, Horváth D, Nánási T, Tóth K, Pothof F, Böhler C, Asplund M, Ruther M, Ulbert I. Long-term recording performance and biocompatibility of chronically implanted cylindrically-shaped, polymer-based neural interfaces. Biomedizinische Technik. 2018;63(3):301–15.
5. Valls-Solé J, Compta Y, Costa J, Valldeoriola F, Rumià J. Human central nervous system circuits examined through the electrodes implanted for deep brain stimulation. Clinical Neurophysiology. 2008; 119(6):1219-31
6. Schrock LE, Mink JW, Woods DW, Porta M, Servello D, Visser-Vandewalle V, Silburn P A, Foltynie T, Walker H C, Shahed-Jimenez J, Savica R, Klassen B T, Machado A G, Foote K D, Zhang JG, Hu W, Ackermans L, Temel Y, Mari Z, K Changizi B K, Lozano A, Auyeung M, Kaido T, Agid Y, Welter M L, Khandhar S M, Mogilner A Y, Pourfar M H, Walter B L, Juncos J L, Gross R E, Kuhn J, F Leckman J F, Neimat J A , Okun M S. Tourette syndrome deep brain stimulation: A review and updated recommendations. Mov Disord. 2015;30(4):448-71
7. Buzsáki G Theta Oscillation of the Hippocampus. Neuron. 2002; 33(3):325-40.
8. Csercsa R, Dombovári B, Fabó D, Wittner L, Erss L, Entz L, Sólyom A, Rásonyi G, Szűcs A, Kelemen A, Jakus R, Juhos V, Grand L, Magony A, Halász P, Freund T F, Maglóczky Z,. Cash S S, Papp L, Karmos G, Halgren E, Ulbert I. Laminar analysis of slow wave activity in humans. Brain. 2010;133(9):2814–29.

9. Wodlinger B, Downey JE, Tyler-Kabara EC, Schwartz AB, Boninger ML, Collinger JL. Ten-dimensional anthropomorphic arm control in a human brain-machine interface: Difficulties, solutions, and limitations. J Neural Eng. 2015;12(1): 016011.
10. Dymond AM, Kaechele LF, Jurist JM, Crandall PH. Brain tissue reaction to some chronically implanted metals. Journal of Neurosurgery. 1970;33(5):574-80.
11. Kotzar G, Freas M, Abel P, Fleischman A, Roy S, Zorman C, Moran J M, Melzak J. Evaluation of MEMS materials of construction for implantable medical devices. Biomaterials. 2002;23(13):2737-50.
12. Zátonyi A, Orbán G, Modi R, Márton G, Meszéna D, Ulbert I, Pongrácz A, Ecker M, Voit W E, Joshi-Imre J, Fekete Z. A softening laminar electrode for recording single unit activity from the rat hippocampus. Sci Rep. 2019;9(1):2321.
13. Kozai TDY, Jaquins-Gerstl AS, Vazquez AL, Michael AC, Cui XT. Brain tissue responses to neural implants impact signal sensitivity and intervention strategies. ACS Chem Neurosci. 2015;6(1):48–67.
14. Hassler C, Boretius T, Stieglitz T. Polymers for neural implants. Journal of Polymer Science, Part B: Polymer Physics. 2011, 49: 18–33.
15. Wang K, Liu CC, Durand DM. Flexible nerve stimulation electrode with iridium oxide sputtered on liquid crystal polymer. IEEE Trans Biomed Eng. 2009;56(1):6–14.
16. Simon D, Ware T, Marcotte R, Lund BR, Smith DW, Di Prima M, Rennaker R L, Voit W. A comparison of polymer substrates for photolithographic processing of flexible bioelectronics. Biomed Microdevices. 2013;15(6):925–39.
17. Grand L, Wittner L, Herwik S, Göthelid E, Ruther P, Oscarsson S, Neves H, Dombovári B, Csercsa R, Karmos G, Ulbert I. Short and long term biocompatibility of NeuroProbes silicon probes. J Neurosci Methods. 2010;189(2):216–29.
18. Voskerician G, Shive MS, Shawgo RS, Von Recum H, Anderson JM, Cima MJ, Langer R. Biocompatibility and biofouling of MEMS drug delivery devices. Biomaterials. 2003;24(11):1959–67.
19. L Nicolelis MA, Dimitrov D, Carmena JM, Crist R, Lehew G, Kralik JD, Wise S P. Chronic, multisite, multielectrode recordings in macaque. Proc Natl Acad Sci U S A. 2003;16;100(19):11041-6.

20. Schuhmann TG, Zhou T, Hong G, Lee JM, Fu TM, Park HG, Lieber C M. Syringe-injectable mesh electronics for stable chronic rodent electrophysiology. Journal of Visualized Experiments. 2018;2018(137).
21. Turner JN, Shain W, Szarowski DH, Andersen M, Martins S, Isaacson M, Cgreaghead B. Cerebral Astrocyte Response to Micromachined Silicon Implants 1999. Exp Neurol. 1999;156(1):33-49
22. Nolta NF, Christensen MB, Crane PD, Skousen JL, Tresco PA. BBB leakage, astrogliosis, and tissue loss correlate with silicon microelectrode array recording performance. Biomaterials. 2015;53:753–62.
23. Henze DA, Borhegyi Z, Csicsvari J, Mamiya A, Harris KD, Buzsáki G. Intracellular Features Predicted by Extracellular Recordings in the Hippocampus In Vivo J Neurophysiol. 2000;84(1):390-400
24. Cohen I, Miles R. Contributions of intrinsic and synaptic activities to the generation of neuronal discharges in in vitro hippocampus. Journal of Physiology 2000; 524(2): 485—502
25. Del Campo A, Greiner C. SU-8: A photoresist for high-aspect-ratio and 3D submicron lithography. Journal of Micromechanics and Microengineering. 2007;17(6):R81-R95.
26. Keller S, Blagoi G, Lillemose M, Haefliger D, Boisen A. Processing of thin SU-8 films. Journal of Micromechanics and Microengineering. 2008;18(12):12520.
27. Rodrigo Martinez-Duarte MJM. SU-8 Photolithography and Its Impacts on Microfludics. In: Microfluidics and Nanofluidics Handbook: Fabrication, Implementation and Applications Editors: Chrakaborthy S,. Mitra S K. Publisher: CRC Press Edition: 1 Chapter: 8 pp.231-268
28. Altuna A, Gabriel G, De La Prida LM, Tijero M, Guimerá A, Berganzo J, Salido R, Villa R, Fernández L J. SU-8-based microneedles for in vitro neural applications. J. Micromech. Microeng. 2010;20(6): 064014.
29. Altuna A, Bellistri E, Cid E, Aivar P, Gal B, Berganzo J, Gabriel G, Guimerà A, Villa R,. FernándezL J, Menendez de la Prida L. SU-8 based microprobes for simultaneous neural depth recording and drug delivery in the brain. Lab Chip. 2013;13(7):1422–30.
30. Márton G, Kiss M, Orbán G, Pongrácz A, Ulbert I. A polymer-based spiky microelectrode array for electrocorticography. Microsystem Technologies. 2015 ;21(3):619–24.

31. Ejserholm F, Köhler P, Bengtsson M, Jorntell H, Schouenborg J, Wallman L. A Polymer Based Electrode Array for Recordings in the Cerebellum. Proceedings of the 5th International IEEE EMBS Conference on Neural Engineering. 2011; 376-9
32. Cho SH, Lu HM, Cauller L, Romero-Ortega MI, Lee JB, Hughes GA. Biocompatible SU-8-based microprobes for recording neural spike signals from regenerated peripheral nerve fibers. IEEE Sens J. 2008;8(11):1830–6.
33. Altuna A, Berganzo J, Fernández LJ. Polymer SU-8-based microprobes for neural recording and drug delivery. Lab Chip, 2013;13:1422-30.
34. Fernandez LJ, Altuna A, Tijero M, Gabriel G, Villa R, Rodríguez MJ, Batlle M, Vilares R, Berganzo J, Blanco F J. Study of functional viability of SU-8-based microneedles for neural applications. Journal of Micromechanics and Microengineering. 2009;19(2): 025007.
35. Bêche B, Pelletier N, Gaviot E, Zyss J. Single-mode TE00-TM00 optical waveguides on SU-8 polymer. Opt Commun. 2004;230(1–3):91–4.
36. Rubehn, Birthe, Wolff, Steffen BE, Tovote, Philip, Schuettler M, Lüthi A, Stieglitz T. Polymer-Based Shaft Microelectrodes with Optical and Fluidic Capabilities As a Tool for Optogenetics. Annu Int Conf IEEE Eng Med Biol Soc. 2011:2969-72.
37. Hennemeyer M, Walther F, Kerstan S, Schürzinger K, Gigler AM, Stark RW. Cell proliferation assays on plasma activated SU-8. Microelectron Eng. 2008;85(5–6):1298–301.
38. Vernekar VN, Cullen DK, Fogleman N, Choi Y, García AJ, Allen MG, Brewer G J, LaPlaca M C. SU-8 2000 rendered cytocompatible for neuronal bioMEMS applications. J Biomed Mater Res A. 2009;89(1):138–51.
39. Nemani K V., Moodie KL, Brennick JB, Su A, Gimi B. In vitro and in vivo evaluation of SU-8 biocompatibility. Materials Science and Engineering C. 2013;33(7):4453–9.
40. Huang SH, Lin SP, Chen JJJ. In vitro and in vivo characterization of SU-8 flexible neuroprobe: From mechanical properties to electrophysiological recording. Sens Actuators A Phys. 2014;216:257–65.
41. Liu J, Fu TM, Cheng Z, Hong G, Zhou T, Jin L, Duvvuri M, Jiang Z, Kruskal P, Xie C, Suo Z, Fang Y, Lieber C M. Syringe-injectable electronics. Nat Nanotechnol. 2015;10(7):629–35.
42. Beghi E. The Epidemiology of Epilepsy. Neuroepidemiology. 2020;54(2):185–91.

43. Thijs RD, Surges R, O’Brien TJ, Sander JW. Epilepsy in adults. The Lancet. 2019;393(10172):689–701.
44. Duncan JS, Sander JW, Sisodiya SM, Walker MC. Adult epilepsy. The Lancet. 2006;367(9516):1087–100.
45. Struck AF, Westover MB. Variability in clinical assessment of neuroimaging in temporal lobe epilepsy. Seizure. 2015;30:132–5.
46. Schmidt D, Schachter SC. Drug treatment of epilepsy in adults. BMJ (Online). 2014;348:g254.
47. Asadi-Pooya AA, Brigo F, Lattanzi S, Blumcke I. Adult epilepsy. The Lancet [Internet]. 2023 Jul;402(10399):412–24. Available from: https://linkinghub.elsevier.com/retrieve/pii/S0140673623010486
48. Jobst BC, Cascino GD. Resective epilepsy surgery for drug-resistant focal epilepsy: A review. JAMA - Journal of the American Medical Association. 2015;313(3):285–93.
49. Mohan M, Keller S, Nicolson A, Biswas S, Smith D, Farah J O, Eldridge P, Wieshmann U. The long-term outcomes of epilepsy surgery. PLoS One. 2018;13(5): e0196274.
50. De Curtis M, Avanzini G. Interictal spikes in focal epileptogenesis Prog Neurobiol. 2001;63(5):541-67.
51. Mccormick DA, Contreras D. On the Cellular and Network Bases of Epileptic Seizures. Annu Rev Physiol. 2001;63:815-46.
52. Avoli M, D’antuono M, Louvel J, Köhling R, Biagini G, Pumain R, D'Arcangelo G, Tancredi V. Network and pharmacological mechanisms leading to epileptiform synchronization in the limbic system in vitro. Prog Neurobiol. 2002;68(3):167-207.
53. Trevelyan AJ, Muldoon SF, Merricks EM, Racca C, Staley KJ. The Role of Inhibition in Epileptic Networks. J Clin. Neuropysiol. 2015;32(3):227-34.
54. Avoli M, Williamsont A. FUNCTIONAL AND PHARMACOLOGICAL PROPERTIES OF HUMAN NEOCORTICAL NEURONS MAINTAINED IN VITRO. Progress in Neurobiology. 1996;48(6):519-54.
55. Avoli M, Louvel J, Pumain R, Köhling R. Cellular and molecular mechanisms of epilepsy in the human brain. Progress in Neurobiology. 2005;77: 166–200.
56. Boldog E, Bakken TE, Hodge RD, Novotny M, Aevermann BD, Baka J, Bordé S, Close JL, Diez-Fuertes F Ding SL, Faragó N, Kocsis ÁK, Kovács B, Maltzer Z, McCorrison JM, Miller JA, Molnár G, Oláh G, Ozsvár A, Rózsa M, Shehata SI, Smith KA, Sunkin

SM, Tran DN, Venepally P, Wall A, Puskás LG, Barzó P, Steemers FJ, Schork NJ, Scheuermann RH, Lasken RS, Lein ES, Tamás G. Transcriptomic and morphophysiological evidence for a specialized human cortical GABAergic cell type. Nat Neurosci. 2018;21(9):1185–95.

57. Zeng H, Shen EH, Hohmann JG, Oh SW, Bernard A, Royall JJ, Glattfelder KJ, Sunkin SM, Morris JA, Guillozet-Bongaarts AL, Smith KA, Ebbert AJ, Swanson B, Kuan L, Page DT, Overly CC, Lein ES, Hawrylycz MJ, Hof PR, Hyde TM, Kleinman JE, Jones AR. Large-scale cellular-resolution gene profiling in human neocortex reveals species-specific molecular signatures. Cell. 2012;149(2):483–96.

58. Mohan H, Verhoog MB, Doreswamy KK, Eyal G, Aardse R, Lodder BN, Goriounova NA, Asamoah B, Brakspear ABCB, Groot C, van der Sluis S, Testa-Silva G, Obermayer J, Boudewijns ZSRM, Narayanan RT, Baayen JC, Segev I, HD, de Kock CPJ. Dendritic and axonal architecture of individual pyramidal neurons across layers of adult human neocortex. Cerebral Cortex. 2015;25(12):4839–53.

59. Beaulieu-Laroche L, Toloza EHS, Brown NJ, Harnett MT. Widespread and Highly Correlated Somato-dendritic Activity in Cortical Layer 5 Neurons. Neuron. 2019;103(2):235-241.

60. Vasile F, Dossi E, Rouach N. Human astrocytes: structure and functions in the healthy brain. Brain Structure and Function. 2017;222: 2017–29.

61. Poorthuis RB, Muhammad K, Wang M, Verhoog MB, Junek S, Wrana A, Mansvelder HD, Letzkus JJ. Rapid Neuromodulation of Layer 1 Interneurons in Human Neocortex. Cell Rep. 2018;23(4):951–8.

62. Eyal G, Verhoog MB, Testa-Silva G, Deitcher Y, Lodder JC, Benavides-Piccione R, Juan Morales,6 Javier DeFelipe,4,5 Christiaan PJ de Kock,2 Huibert D Mansvelder,2 and Idan Segev1,3. Unique membrane properties and enhanced signal processing in human neocortical neurons. Elife. 2016; 5:e16553.

63. Shadlen MN, Newsome WT. Noise, neural codes and cortical organization., Current Opinion in Neurobiology. Curr Opin Neurobiol. 1994;4(4):569-79.

64. Haider B, Duque A, Hasenstaub AR, McCormick DA. Neocortical network activity in vivo is generated through a dynamic balance of excitation and inhibition. Journal of Neuroscience. 2006;26(17):4535–45.

65. Dehghani N, Peyrache A, Telenczuk B, Le Van Quyen M, Halgren E, Cash SS, Hatsopoulos NG, Destexhe A. Dynamic balance of excitation and inhibition in human and monkey neocortex. Sci Rep. 2016;6:23176.
66. Kandrács Á, Hofer KT, Tóth K, Tóth EZ, Entz L, Bagó AG, Erőss L, Jordán Z, Nagy G, Fabó D, Ulbert I, Wittner L. Presence of synchrony-generating hubs in the humanepileptic neocortex. Journal of Physiology. 2019; 597(23):5639-5670.
67. Hofer KT, Kandrács Á, Tóth K, Hajnal B, Bokodi V, Tóth EZ, Erőss L, Entz L, Bagó AG, Fabó D, Ulbert I, Wittner L. Bursting of excitatory cells is linked to interictal epileptic discharge generation in humans. Sci Rep. 2022;12(1):6280.
68. Hofer KT, Kandrács Á, Ulbert I, Pál I, Szabó C, Héja L, Wittner L. The hippocampal CA3 region can generate two distinct types of sharp wave-ripple complexes, in vitro. Hippocampus. 2015 Feb 1;25(2):169–86.
69. Florez CM, McGinn RJ, Lukankin V, Marwa I, Sugumar S, Dian J, Hazrati LN, Carlen PL, Zhang L, Valiante TA. In vitro recordings of human neocortical oscillations. Cerebral Cortex. 2015;25(3):578–97.
70. Köhling R, Lücke A, Straub H, Speckmann EJ, Tuxhorn I, Wolf P, Pannek H,Oppel S. Spontaneous sharp waves in human neocortical slices excised from epileptic patients. Brain. 1998;121 (Pt 6):1073-87
71. Pallud J, Le Van Quyen M, Bielle F, Pellegrino C, Varlet P, Baulac M, Duyckaerts C, Kourdougli N, Chazal G, Devaux B, Rivera C, Miles R, Capelle L, Huberfeld G. Cortical GABAergic excitation contributes to epileptic activities around human glioma. Sci Transl Med. 2014 ;6(244):89.
72. Molnár G, Oláh S, Komlósi G, Füle M, Szabadics J, Varga C, Barzó P, Tamás G. Complex Events Initiated by Individual Spikes in the Human Cerebral Cortex. PLoS Biol. 6(9):e222.
73. Tóth K, Hofer KT, Kandrács Á, Entz L, Bagó A, Erőss L, Bagó A, Erőss L, Jordán Z, Nagy G, Sólyom A, Fabó D, Ulbert I, Wittner L. Hyperexcitability of the network contributes to synchronization processes in the human epileptic neocortex. Journal of Physiology. 2018;596(2):317–42.
74. Kerekes BP, Tóth K, Kaszás A, Chiovini B, Szadai Z, Szalay G, Pálfi D, Bagó A, Spitzer K, Rózsa B, Ulbert I, Wittner L. Combined two-photon imaging

electrophysiological, and anatomical investigation of the human neocortex in vitro . Neurophotonics. 2014;1(1):011013.

75. Szegedi V, Paizs M, Csakvari E, Molnar G, Barzo P, Tamas G, Lamsa K. Plasticity in Single Axon Glutamatergic Connection to GABAergic Interneurons Regulates Complex Events in the Human Neocortex. PLoS Biol. 2016;14(11).
76. Miles R, Tó K, Attila †, Gulyá I. Differences between Somatic and Dendritic Inhibition in the Hippocampus. Neuron. 1996 Apr;16(4):815-23.
77. Freund TF, Katona I. Perisomatic Inhibition. Neuron. 2007;55:33–42.
78. Seress L, Gulyás AI, Ferrer I, Tunon T, Soriano E, Freund TF. Distribution, morphological features, and synaptic connections of parvalbumin- and calbindin D28k-immunoreactive neurons in the human hippocampal formation. Journal of Comparative Neurology. 1993;337(2):208–30.
79. Freund TF, Buzsáki G. Interneurons of the Hippocampus. Hippocampus. 1996;6(4):347–470.
80. Freund TF. Interneuron Diversity series: Rhythm and mood in perisomatic inhibition. Trends in Neurosciences. 2003;26:489–95.
81. Hájos N, Karlócai MR, Németh B, Ulbert I, Monyer H, Szabó G, Erdélyi F, Freund TF, Gulyás AI. Input-output features of anatomically identified CA3 neurons during hippocampal sharp wave/ripple oscillation in vitro. Journal of Neuroscience. 2013;33(28):11677–91.
82. Gulyás AI, Freund TT. Generation of physiological and pathological high frequency oscillations: The role of perisomatic inhibition in sharp-wave ripple and interictal spike generation. Current Opinion in Neurobiology. 2015;31:26–32.
83. Menendez de la Prida L, Trevelyan AJ. Cellular mechanisms of high frequency oscillations in epilepsy: On the diverse sources of pathological activities. Epilepsy Res. 2011;97(3):308–17.
84. Maglóczky Z, Freund TF. Impaired and repaired inhibitory circuits in the epileptic human hippocampus. Trends in Neurosciences. 2005;28: 334–40.
85. Ma Y, Prince DA. Functional alterations in GABAergic fast-spiking interneurons in chronically injured epileptogenic neocortex. Neurobiol Dis. 2012;47(1):102–13.
86. Kohus Z, Káli S, Rovira-Esteban L, Schlingloff D, Papp O, Freund TF, Hájos N, Gulyás AI. Properties and dynamics of inhibitory synaptic communication within the CA3

microcircuits of pyramidal cells and interneurons expressing parvalbumin or cholecystokinin. Journal of Physiology. 2016;594(13):3745–74.

87. Szabó GG, Holderith N, Gulyás AI, Freund TF, Hájos N. Distinct synaptic properties of perisomatic inhibitory cell types and their different modulation by cholinergic receptor activation in the CA3 region of the mouse hippocampus. European Journal of Neuroscience. 2010;31(12):2234–46.
88. Klausberger T, Somogyi P. Neuronal diversity and temporal dynamics: The unity of hippocampal circuit operations. Science. 2008;321:53–7.
89. Klausberger T, Marton LF, O'Neill J, Huck JHJ, Dalezios Y, Fuentealba P, Suen WY, Papp E, Kaneko T, Watanabe M, Csicsvari J, Somogyi P. Complementary roles of cholecystokinin- and parvalbumin-expressing GABAergic neurons in hippocampal network oscillations. Journal of Neuroscience. 2005;25(42):9782–93.
90. Karlócai MR, Kohus Z, Káli S, Ulbert I, Szabó G, Máté Z, Freund TF, Gulyás AI. Physiological sharp wave-ripples and interictal events in vitro: What's the difference? Brain. 2014;137(2):463–85.
91. Van Brederode JFM, Helliesen M Il, Hendrickson AE. Distribution of the Calcium-binding Proteins Parvalbumin and Calbindin-D28k in the Sensorimotor Cortex of the Rat. Neuroscience. 1991;44(1):157-71.
92. DeFelipe J, Garcia Sola R, Marco P, del Rosario del Rio M, Pulido P, Cajal R S. Selective Changes in the Microorganization of the Human Epileptogenic Neocortex Revealed by Pan/albumin Immunoreactivity Cereb Cortex. 1993;3(1):39-48
93. Del Rio A R, Defelipe J. A Study of SMI 32-Stained Pyramidal Cells, Parvalbumin-Immunoreactive Chandelier Cells, and Presumptive Thalamocortical Axons in the Human Temporal Neocortex., The Journal of Comparative Neurology. 1994;342(3):389-408
94. Wittner L, Eross L, Czirják S, Halász P, Freund TF, Maglóczky Z. Surviving CA1 pyramidal cells receive intact perisomatic inhibitory input in the human epileptic hippocampus. Brain. 2005;128(1):138–52.
95. Wittner L, Huberfeld G, Clémenceau S, Erss L, Dezamis E, Entz L, Ulbert I, Baulac M, Freund TF, Maglóczky Z, Miles R. The epileptic human hippocampal cornu ammonis 2 region generates spontaneous interictal-like activity in vitro. Brain. 2009;132(11):3032–46.

,

96. Wittner L, Maglóczky Z, Borhegyi Z, Halász PS, Tóth S, Erőss L,Szabó Z, Freund T F. Preservation of Perisomaitc Inhibitory Input of Granule Cells in the Epileptic Human Dentate Gyrus. Neuroscience. 2001;108(4):587-600
97. Wittner L, Maglóczky Z. Synaptic Reorganization of the Perisomatic Inhibitory Network in Hippocampi of Temporal Lobe Epileptic Patients. BioMed Research International. 2017; 7154295.
98. Zamecnik J, Krsek P, Druga R, Marusic P, Benes V, Tichy M, Komarek V. Densities of parvalbumin-immunoreactive neurons in non-malformed hippocampal sclerosis-temporal neocortex and in cortical dysplasias. Brain Res Bull. 2006;68(6):474–81.
99. Pilar Marco JD. Altered synaptic circuitry in the human temporal neocortex removedfrom epileptic patients. Exp Brain Res. 1997;(114):1–10.
100. Marco P, Sola RG, y Cajal SR, Defelipe J. Loss of Inhibitory Synapses on the Soma and Axon Initial Segment of Pyramidal Cells in Human Epileptic Peritumoural Neocortex: Implications for Epilepsy. Brain Research Bulletin. 1997; 44(1):47-66.
101. Katona I, Urbán GM, Wallace M, Ledent C, Jung KM, Piomelli D, Mackie K, Freund TF. Molecular composition of the endocannabinoid system at glutamatergic synapses. Journal of Neuroscience. 2006;26(21):5628–37.
102. Eggan SM, Lewis DA. Immunocytochemical distribution of the cannabinoid CB1 receptor in the primate neocortex: A regional and laminar analysis. Cerebral Cortex. 2007;17(1):175–91.
103. Ludányi A, Eross L, Czirják S, Vajda J, Halász P, Watanabe M, Palkovits M, Maglóczky Z, Freund TF, Katona I. Downregulation of the CB1 cannabinoid receptor and related molecular elements of the endocannabinoid system in epileptic human hippocampus. Journal of Neuroscience. 2008;28(12):2976–90.
104. Maglóczky Z, Tóth K, Karlócai R, Nagy S, Eross L, Czirják S, Vajda J, Rásonyi G, Kelemen A, Juhos V, Halász P, Mackie K, Freund TF. Dynamic changes of CB1-receptor expression in hippocampi of epileptic mice and humans. Epilepsia. 2010; 51 Suppl 3(Suppl 3):115-20.
105. Zurolo E, Iyer AM, Spliet WGM, Van Rijen PC, Troost D, Gorter JA, Aronica E. CB1 and CB2 cannabinoid receptor expression during development and in epileptogenic developmental pathologies. Neuroscience. 2010;170(1):28–41.

106. Hasselmo ME. The role of acetylcholine in learning and memory. Current Opinion in Neurobiology. 2006;16(6):710-5.

107. Schliebs R, Arendt T. The significance of the cholinergic system in the brain during aging and in Alzheimer's disease. Journal of Neural Transmission. 2006;113:1625–44.

108. Schliebs R, Arendt T. The cholinergic system in aging and neuronal degeneration. Behavioural Brain Research. 2011;221:555–63.

109. Alkondon M, Albuquerque EX. The nicotinic acetylcholine receptor subtypes and their function in the hippocampus and cerebral cortex. Progress in Brain Research. 2004; 145:109-20.

110. Fabian-Fine R, Skehel P, Errington ML, Davies HA, Sher E, Stewart MG, Fine A. Ultrastructural Distribution of the 7 Nicotinic Acetylcholine Receptor Subunit in Rat Hippocampus. J Neurosci. 2001;21(20):7993-8003.

111. Obermayer J, Verhoog MB, Luchicchi A, Mansvelder HD. Cholinergic modulation of cortical microcircuits is layer-specific: Evidence from rodent, monkey and human brain. Frontiers in Neural Circuits. 2017;11:100.

112. Brown DA. Muscarinic acetylcholine receptors (mAChRs) in the nervous system: Some functions and mechanisms., Journal of Molecular Neuroscience. 2010;41:340–6.

113. Gulledge AT, Stuart GJ. Cholinergic inhibition of neocortical pyramidal neurons. Journal of Neuroscience. 2005;25(44):10308–20.

114. Dasari S, Hill C, Gulledge AT. A unifying hypothesis for M1 muscarinic receptor signalling in pyramidal neurons. Journal of Physiology. 2017 595(5):1711–23.

115. Krnjevj K, Pumain R, Renaudt L. The Mechanism of Excitation by Acetylcholine in the Cerebral Coertex. J. Physiol. 1971; 215(1): 247–268.

116. Lawrence JJ. Cholinergic control of GABA release: emerging parallels between neocortex and hippocampus. Trends in Neurosciences. 2008;31:317–27.

117. Salgado H, Bellay T, Nichols JA, Bose M, Martinolich L, Perrotti L, et al. Muscarinic M2 and M1 receptors reduce GABA release by Ca2+ channel modulation through activation of PI3K/ Ca2+-independent and PLC/Ca2+-dependent PKC. J Neurophysiol. 2007;98(2):952–65.

118. Disney AA, Reynolds JH. Expression of m1-type muscarinic acetylcholine receptors by parvalbumin-immunoreactive neurons in the primary visual cortex: A comparative

study of rat, guinea pig, ferret, macaque, and human. Journal of Comparative Neurology. 2014;522(5):986–1003.

119. Fukudome Y, Ohno-Shosaku T, Matsui M, Omori Y, Fukaya M, Tsubokawa H, Taketo MM, Watanabe M, Manabe T, Kano M. Two distinct classes of muscarinic action on hippocampal inhibitory synapses: M2-mediated direct suppression and M1/M3-mediated indirect suppression through endocannabinoid signalling. European Journal of Neuroscience. 2004;19(10):2682–92.

120. Freund AF, Katona A, Piomelli D. Role of Endogenous Cannabinoids in Synaptic Signaling. Physil Rev. 2003 Jul;83(3):1017-66.

121. Katona I, Sperlágh B, SíkA, Käfalvi A, Vizi E S, Mackie K, Freund T F. Presynaptically Located CB1 Cannabinoid Receptors Regulate GABA Release from Axon Terminals of Specific Hippocampal Interneurons. J Neurosci. 1999;19(11):4544-58

122. Kovacs FE, Knop T, Urbanski MJ, Freiman I, Freiman TM, Feuerstein TJ, Zentner J, SzaboB. Exogenous and endogenous cannabinoids suppress inhibitory neurotransmission in the human neocortex., Neuropsychopharmacology. 2012;37:1104–14.

123. Mackie K. Signaling via CNS Cannabinoid Receptors. Mol Cell Endocrinol. 2008;286(1-2 Suppl 1):S60-5

124. Hamilton SE, Loose MD, Qi M, Levey AI, Hille B, Mcknight GS, Idzerda R L, Nathanson N M. Disruption of the m1 receptor gene ablates muscarinic receptor-dependent M current regulation and seizure activity in mice Proc Natl Acad Sci U S A. 1997;94(24):13311-6

125. Bymaster FP, Carter PA, Yamada M, Gomeza J, Wess J, Hamilton SE, Nathanson NM, McKinzie DL, Felder CC. Role of specific muscarinic receptor subtypes in cholinergic parasympathomimetic responses, in vivo phosphoinositide hydrolysis, and pilocarpine-induced seizure activity. European Journal of Neuroscience. 2003;17(7):1403–10.

126. Gigout S, Wierschke S, Lehmann TN, Horn P, Dehnicke C, Deisz RA. Muscarinic acetylcholine receptor-mediated effects in slices from human epileptogenic cortex. Neuroscience. 2012;223:399–411.

127. Carr DB, Surmeier DJ. M1 muscarinic receptor modulation of Kir2 channels enhances temporal summation of excitatory synaptic potentials in prefrontal cortex pyramidal neurons. J Neurophysiol. 2007;97(5):3432–8.
128. Gigout S, Jones GA, Wierschke S, Davies CH, Watson JM, Deisz RA. Distinct muscarinic acetylcholine receptor subtypes mediate pre-and postsynaptic effects in rat neocortex BMC Neurosci. 2012;13:42
129. Auerbach JM, Segal M. Muscarinic receptors mediating depression and long-term potentiation in rat hippocampus. Journal of Physiology. 1996; 492 (2):479-93.
130. Altiere R J , Travis D C, Roberts J, Thompson D C. Pharmacological characterization of muscarinic receptors mediating acetylcholine-induced contraction and relaxation in rabbit intrapulmonary arteries. J Pharmacol Exp Ther. 1994;270(1):269-76
131. Giang M, Papamatheakis DG, Nguyen D, Paez R, Blum Johnston C, Kim J Brunnell A, Blood Q, Goyal R, Longo LD, Wilson SM. Muscarinic Receptor Activation Affects Pulmonary Artery Contractility in Sheep: The Impact of Maturation and Chronic Hypoxia on Endothelium-Dependent and Endothelium-Independent Function. High Alt Med Biol. 2016;17(2):122–32.
132. Jos NH, Papp EC, Acsa LD, Levey AI, Freund TF. Distincr Interneuron Types Express M2 Muscarinic Receptor Immunoreactivity on their Dendrites or Axon Terminals in the Hippocampus. Neuroscience. 1998;82(2):355-76.
133. Chaudhuri JD, Hiltunen M, Nykänen M, Ylä-Herttuala S, Soininen H, Miettinen R. Localization of M2 muscarinic receptor protein in parvalbumin and calretinin containing cells of the adult rat entorhinal cortex using two complementary methods. Neuroscience. 2005;131(2):557–66.
134. Gatley SJ, Lan R, Pyattl B, Giffordl AN, Volkowl ND, Makriyannis A. Binding of the Non-Classical Cannabinoid CP 55,940, and the Diarylpyrazole AM251 to Rodent Brain Cannabinoid Receptors. Life Sci. 1997;61(14):PL 191-7.
135. Pagotto U, Marsicano G, Cota D, Lutz B, Pasquali R. The Emerging Role of the Endocannabinoid System in Endocrine Regulation and Energy Balance. Endocr Rev. 2006;27(1):73–100.
136. Jordan CJ, Xi ZX. Progress in brain cannabinoid CB 2 receptor research: From genes to behavior. Neuroscience and Biobehavioral Reviews. 2019;98:208-220

137. Chou S, Ranganath T, Fish KN, Lewis DA, Sweet RA. Cell type specific cannabinoid CB1 receptor distribution across the human and non-human primate cortex. Sci Rep. 2022;12(1):9605.
138. Ulbert I, Halgren E, Heit G, Karmos G. Multiple microelectrode-recording system for human intracortical applications J Neurosci Methods. 2001;106(1):69-79
139. Herreras O. Local field potentials: Myths and misunderstandings. Front Neural Circuits. 2016;10:101.
140. Scherberger H. Neural Prostheses for Reaching. In: Encyclopedia of Neuroscience. Elsevier; 2009; p. 213–20.
141. Sofroniew M V., Vinters H V. Astrocytes: Biology and pathology. Acta Neuropathologica. 2010; 119(1):7-35.
142. Gould E , Reeves A J, Graziano M S, Gross C G. Neurogenesis in the Neocortex of Adult Primates. Science . 1999;286(5439):548-52.
143. Mullen RJ, Buck CR, Smith AM. NeuN, a neuronal specific nuclear protein in vertebrates. Development. 1992;116:201-11.
144. Márton G, Tóth EZ, Wittner L, Fiáth R, Pinke D, Orbán G, Meszéna D, Pál I, Győri EL, Bereczki Z, Kandrács Á, Hofer KT, Pongrácz A, Ulbert I, Tóth K. The neural tissue around SU-8 implants: A quantitative in vivo biocompatibility study. Materials Science and Engineering C. 2020;112 :110870.
145. Salatino JW, Ludwig KA, Kozai TDY, Purcell EK. Glial responses to implanted electrodes in the brain. Nat Biomed Eng. 2017;1(11):862–77.
146. Hájos N, Papp EC, Acsády L, Levey AI, Freund TF. Distinct interneuron types express m2 muscarinic receptor immunoreactivity on their dendrites or axon terminals in the hippocampus. Neuroscience. 1997;82(2):355–76.
147. Marsicano G, Lutz B. Expression of the cannabinoid receptor CB1 in distinct neuronal subpopulations in the adult mouse forebrain. European Journal of Neuroscience. 1999;11(12):4213–25.
148. Lorenz H, Despont M, Fahrni N, Labianca N, Renaud P, Vettiger P. SU-8: a low-cost negative resist for MEMS. J. Micromech. Microeng. 1997;7:121-124.
149. Matarèse BFE, Feyen PLC, Falco A, Benfenati F, Lugli P, Demello JC. Use of SU8 as a stable and biocompatible adhesion layer for gold bioelectrodes. Sci Rep. 2018;8(1).

150. Stangegaard M, Wang Z, Kutter JP, Dufva M, Wolff A. Whole genome expression profiling using DNA microarray for determining biocompatibility of polymeric surfaces. Mol Biosyst. 2006;2(9):421–8.
151. Ahmed Z, Reddy JW, Malekoshoaraie MH, Hassanzade V, Kimukin I, Jain V, et al. Flexible optoelectric neural interfaces. Vol. 72, Current Opinion in Biotechnology. Elsevier Ltd; 2021. p. 121–30.
152. Chen Z, Lee JB. Biocompatibility of su-8 and its biomedical device applications. Vol. 12, Micromachines. MDPI AG; 2021.
153. Golvari P, Kuebler SM. Fabrication of functional microdevices in su-8 by multi-photon lithography. Vol. 12, Micromachines. MDPI AG; 2021.
154. Rousche PJ, Normann RA. Chronic recording capability of the Utah Intracortical Electrode Array in cat sensory cortex. Vol. 82, Journal of Neuroscience Methods. 1998.
155. Williams JC, Rennaker RL, Kipke DR. Long-term neural recording characteristics of wire microelectrode arrays implanted in cerebral cortex Brain Res Brain Res Protoc. 1999;4(3):303-13
156. Liu X, Mccreery DB, Carter RR, Bullara LA, Yuen TGH, Agnew WF. Stability of the Interface Between Neural Tissue and Chronically Implanted Intracortical Microelectrodes. IEEE Trans Rehabil Eng. 1999;7(3):315-26
157. Biran R, Martin DC, Tresco PA. Neuronal cell loss accompanies the brain tissue response to chronically implanted silicon microelectrode arrays. Exp Neurol. 2005;195(1):115–26.
158. McConnell GC, Rees HD, Levey AI, Gutekunst CA, Gross RE, Bellamkonda R V. Implanted neural electrodes cause chronic, local inflammation that is correlated with local neurodegeneration. J Neural Eng. 2009;6(5).
159. Winslow BD, Tresco PA. Quantitative analysis of the tissue response to chronically implanted microwire electrodes in rat cortex. Biomaterials. 2010;31(7):1558–67.
160. Bérces Z, Tóth K, Márton G, Pál I, Kováts-Megyesi B, Fekete Z, et al. Neurobiochemical changes in the vicinity of a nanostructured neural implant. Sci Rep. 2016;6.
161. Schultz RL, Willey TJ. The ultrastructure of the sheath around chronically implanted electrodes in brain. Vol. 5, Journal of Neurocytology. 1976.

162. Ludwig KA, Uram JD, Yang J, Martin DC, Kipke DR. Chronic neural recordings using silicon microelectrode arrays electrochemically deposited with a poly(3,4ethylenedioxythiophene) (PEDOT) film. J Neural Eng. 2006;3(1):59–70.
163. Merrill DR, Tresco PA. Impedance characterization of microarray recording electrodes in vitro. IEEE Trans Biomed Eng. 2005;52(11):1960–5.
164. Vetter RJ, Williams JC, Hetke JF, Nunamaker EA, Kipke DR. Chronic neural recording using silicon-substrate microelectrode arrays implanted in cerebral cortex. IEEE Trans Biomed Eng. 2004;51(6):896–904.
165. Schmidt S, Horch K, Normann R. Biocompatibility of silicon-based electrode arrays implanted in feline cortical tissue.
166. Purcell EK, Thompson DE, Ludwig KA, Kipke DR. Flavopiridol reduces the impedance of neural prostheses in vivo without affecting recording quality. J Neurosci Methods. 2009;183(2):149–57.
167. McCreery D, Cogan S, Kane S, Pikov V. Correlations between histology and neuronal activity recorded by microelectrodes implanted chronically in the cerebral cortex. J Neural Eng. 2016;13(3).
168. Saxena T, Karumbaiah L, Gaupp EA, Patkar R, Patil K, Betancur M, Stanley GB, Bellamkonda RV. The impact of chronic blood-brain barrier breach on intracortical electrode function. Biomaterials. 2013;34(20):4703–13.
169. Edell DJ, Van Toi V, McNeil VM, Clark LD. Factors Influencing the Biocompatibility of Insertable Silicon Microshafts in Cerebral Cortex. IEEE Trans Biomed Eng. 1992;39(6):635-43
170. Azemi E, Lagenaur CF, Cui XT. The surface immobilization of the neural adhesion molecule L1 on neural probes and its effect on neuronal density and gliosis at the probe/tissue interface. Biomaterials. 2011;32(3):681–92.
171. Joseph K, Kirsch M, Johnston M, Münkel C, Stieglitz T, Haas CA, Hofmann UG. Transcriptional characterization of the glial response due to chronic neural implantation of flexible microprobes. Biomaterials. 2021;279:121230.
172. Sloviter RS. Permanently Altered Hippocampal Structure, Excitability, and Inhibition After Experimental Status Epilepticus in the Rat: The “Dormant Basket Cell” Hypothesis and its Possible Relevance to Temporal Lobe Epilepsy. Vol. 1, Hippocampus. 1991; 1(1):41-66

173. Bekenstein JW, Lothman EW. Dormancy of Inhibitory Interneurons in a Model of Temporal Lobe Epilepsy Science 1993;259(5091):97-100

174. Bernard C, Esclapez M, Hirsch JC, Ben-Ari Y. Interneurones are not so dormant in temporal lobe epilepsy: a critical reappraisal of the dormant basket cell hypothesis. Epilepsy Res. 1998;32(1-2):93-103.

175. Cox JA, Winge DR, Stein EA. Calcium, magnesium and the conformation of parvalbumin during muscular activity. Biochimie. 1979;61(5–6):601–5.

176. Blancuzzi Y, Padilla A, Cave A, Parello J. Symmetrical rearrangement of the cation-binding sites of parvalbumin upon calcium/magnesium exchange. A study by proton 2D NMR. Biochemistry. 1993;32(5):1302–9.

177. Johansen La FF, Tonder N, Zimmer J, Baimbridge KG, Diemer NH. Short-term changes of parvalbumin and calbindin immunoreactivity in the rat hippocampus following cerebral ischemia. Neuroseience Letters. 1990; 120(2):171-4

178. Curia G, Lucchi C, Vinet J, Gualtieri F, Marinelli C, Torsello A, et al. Pathophysiogenesis of Mesial Temporal Lobe Epilepsy: Is Prevention of Damage Antiepileptogenic? Curr Med Chem. 2014;21(6):663–88.

180. Maglóczky Z. Sprouting in human temporal lobe epilepsy: Excitatory pathways and axons of interneurons. Epilepsy Res. 2010;89(1):52–9.

181. Lein ES, Zhao X, Gage FH. Defining a Molecular Atlas of the Hippocampus Using DNA Microarrays and High-Throughput In Situ Hybridization. Journal of Neuroscience. 2004;24(15):3879–89.

182. Yuste R, Hawrylycz M, Aalling N, Aguilar-Valles A, Arendt D, Armañanzas R, Ascoli GA, Bielza C, Bokharaie V, Borgtoft Bergmann T, Bystron I, Capogna M, Chang YJ, Clemens A, de Kock CPJ, DeFelipe J, Dos Santos SE, Dunville K, Feldmeyer D, Fiáth R, Fishell GJ, Foggetti A, Gao X, Ghaderi X, Goriounova NA, Güntürkün O, Hagihara K, Hall VJ, Helmstaedter M, Herculano-Houzel S, Hilscher MM, Hirase H, Hjerling-Leffler J, Hodge R, Huang J, Huda R, Khodosevich K, Kiehn O, Koch H, Kuebler ES, Kühnemund M, Larrañaga P, Lelieveldt B, Louth EL, Lui JH, Mansvelder HD, Marin O, Martinez-Trujillo J, Chameh HM, Mohapatra AN, Munguba H, Nedergaard M, Němec P, Ofer N, Pfisterer UG, Pontes S, Redmond W, Rossier J, Sanes JR, Scheuermann RH, Serrano-Saiz E, Staiger JF, Somogyi P, Tamás G, Tolias AS, Tosches MA, García MT, Wozny C, Wuttke TV, Liu Y, Yuan J, Zeng HJ, Lein e. A

community-based transcriptomics classification and nomenclature of neocortical cell types. Nature Neuroscience. 2020;23(12):1456-1468

183. Mercer A, Thomson AM. Cornu ammonis regions-antecedents of cortical layers? Frontiers in Neuroanatomy. 2017;11:83

184. Schlingloff D, Káli S, Freund TF, Hájos N, Gulyás AI. Mechanisms of sharp wave initiation and ripple generation. Journal of Neuroscience. 2014;34(34):11385–98.

185. Schwartzkroin PA. Cellular electrophysiology of human epilepsy. Epilepsy Res. 199;17(3):185-92.

186. Kozai TDY, Marzullo TC, Hooi F, Langhals NB, Majewska AK, Brown EB, Kipke RD. Reduction of neurovascular damage resulting from microelectrode insertion into the cerebral cortex using in vivo two-photon mapping. J Neural Eng. 2010;7(4):046011.

187. Holderith N, Lorincz A, Katona G, Rózsa B, Kulik A, Watanabe M, Nusser Z. Release probability of hippocampal glutamatergic terminals scales with the size of the active zone. Nat Neurosci. 2012;15(7):988–97.

9. Bibliography

9.1 Connected to the Thesis

EZ Tóth, FG Szabó, Á Kandrács, N Molnár, G Nagy, AG Bagó, L Erőss, Dániel Fabó, Boglárka Hajnal, Bence Rácz, Lucia Wittner, István Ulbert, Kinga Tóth, *Perisomatic Inhibition and Its Relation to Epilepsy and to Synchrony Generation in the Human Neocortex*
International Journal of Molecular Sciences, 2022, 23 (1)

Gergely Márton, Estilla Zsófia Tóth, Lucia Wittner, Richárd Fiáth, Domonkos Pinke, Gábor Orbán, Domokos Meszéna, Ildikó Pál, Edit Lelle Győri, Zsófia Bereczki, Ágnes Kandrács, Katharina T Hofer, Anita Pongrácz, István Ulbert, Kinga Tóth, *The neural tissue around SU-8 implants: A quantitative in vivo biocompatibility study* Materials Science and Engineering: C 112, 110870, 2020

9.2 Not Connected to the Thesis

Dénes Szepesi Kovács, Balázs Chiovini, Dalma Müller, Estilla Zsófia Tóth, Anna Fülöp, Péter Ábrányi-Balogh, Lucia Wittner, György Várady, Ödön Farkas, Gábor Turczel, Gergely Katona, Balázs Győrffy, György Miklós Keserű, Zoltán Mucsi, Balázs J. Rózsa, and Ervin Kovács, Synthesis and Application of Two-Photon Active Fluorescent Rhodol Dyes for Antibody Conjugation and In Vitro Cell Imaging, ACS Omega 2023. Jun 14., 8, 25, 22836–22843

Katharina T Hofer, Ágnes Kandrács, Kinga Tóth, Boglárka Hajnal, Virág Bokodi, Estilla Zsófia Tóth, Loránd Erőss, László Entz, Attila G Bagó, Dániel Fabó, István Ulbert, Lucia Wittner *Bursting of excitatory cells is linked to interictal epileptic discharge generation in humans,* Scientific Reports, 2022, 12 (1), 6280

Dénes Szepesi Kovács, Imre Hajdu, Gergely Mészáros, Lucia Wittner, Domokos Meszéna, Estilla Zsófia Tóth, Zita Hegedűs, Ivan Ranđelović, József Tóvári, Tímea

Szabó, Bence Szilágyi, Mátyás Milen, György Miklós Keserű, Péter Ábrányi-Balogh *Synthesis and characterization of new fluorescent boro-β-carboline dyes* RSC advances 11 (21), 2021 12802-12807

Petri L, Ábrányi-Balogh P, Vagrys D, Imre T, Varró N, Mándity I, Rácz A, Wittner L, Tóth K, Tóth EZ, Juhász T, Davis B, Keserű GM. A covalent strategy to target intrinsically disordered proteins: Discovery of novel tau aggregation inhibitors. Eur J Med Chem. 2022 Mar 5;231:114163. doi: 10.1016/j.ejmech.2022.114163

Bors L, Tóth K, Tóth EZ, Bajza Á, Csorba A, Szigeti K, Máthé D, Perlaki G, Orsi G, Tóth GK, Erdő F. Corrigendum to "Age-dependent changes at the blood-brain barrier. A comparative structural and functional study in young adult and middle aged rats" [Brain Res. Bull. 139C (2018) 269-277]. Brain Res Bull. 2020 Feb;155:211-212

Kandrács Á, Hofer KT, Tóth K, Tóth EZ, Entz L, Bagó AG, Erőss L, Jordán Z, Nagy G, Fabó D, Ulbert I, Wittner L. Presence of synchrony-generating hubs in the human epileptic neocortex. J Physiol. 2019 Oct 10 ;597(23):5639-5670.

Bors L, Tóth K, Tóth EZ, Bajza Á, Csorba A, Szigeti K, Máthé D, Perlaki G, Orsi G, Tóth GK, Erdő F. Age-dependent changes at the blood-brain barrier. A Comparative structural and functional study in young adult and middle aged rats. Brain Res Bull. 2018 Mar 6, 139:269-277.

10. Acknowledgments

I would like to thank the patients and their families to let us carry out this research.

I would like to thank supervision and care for my supervisor Lucia Wittner.

I would like to thank from the help from everybody in the Integrative Neuroscience Research Group and for the Neurologist and neurosurgeons from OMIII.

Also, I would like to mention the members of the Institute of Cognitive Neuroscience and Psychology who have helped.